The Astrophysical Journal, 803:26 (24pp), 2015 April 10 doi:10.1088/0004-637X/803/1/26
© 2015. The American Astronomical Society. All rights reserved.

ZFOURGE/CANDELS: ON THE EVOLUTION OF M^* GALAXY PROGENITORS FROM $z = 3$ TO 0.5*

C. Papovich[1,2], I. Labbé[3], R. Quadri[1,2,28], V. Tilvi[1,2], P. Behroozi[4], E. F. Bell[5], K. Glazebrook[6], L. Spitler[7,8], C. M. S. Straatman[3], K.-V. Tran[1,2], M. Cowley[7], R. Davé[9,10,11], A. Dekel[12], M. Dickinson[13], H. C. Ferguson[4], S. L. Finkelstein[14], E. Gawiser[15], H. Inami[13], S. M. Faber[16], G. G. Kacprzak[6,29], L. Kawinwanichakij[1,2], D. Kocevski[17], A. Koekemoer[4], D. C. Koo[16], P. Kurczynski[15], J. M. Lotz[4], Y. Lu[18], R. A. Lucas[4], D. McIntosh[19], N. Mehrtens[1,2], B. Mobasher[20], A. Monson[21], G. Morrison[22,23], T. Nanayakkara[6], S. E. Persson[21], B. Salmon[1,2], R. Simons[24], A. Tomczak[1,2], P. van Dokkum[25], B. Weiner[26], and S. P. Willner[27]

[1] George P. and Cynthia Woods Mitchell Institute for Fundamental Physics and Astronomy, Texas A&M University, College Station, TX 77843-4242, USA
[2] Department of Physics and Astronomy, Texas A&M University, College Station, TX 77843-4242, USA; papovich@tamu.edu
[3] Leiden Observatory, Leiden University, P.O. Box 9513, NL-2300 RA Leiden, The Netherlands
[4] Space Telescope Science Institute, 3700 San Martin Drive, Baltimore, MD 21218, USA
[5] Department of Astronomy, University of Michigan, Ann Arbor, MI 48109, USA
[6] Centre for Astrophysics & Supercomputing, Swinburne University, Hawthorn, VIC 3122, Australia
[7] Department of Physics & Astronomy, Macquarie University, Sydney, NSW 2109, Australia
[8] Australian Astronomical Observatory, 105 Delhi Road, Sydney, NSW 2113, Australia
[9] University of the Western Cape, Bellville, Cape Town 7535, South Africa
[10] South African Astronomical Observatories, Observatory, Cape Town 7925, South Africa
[11] African Institute for Mathematical Sciences, Muizenberg, Cape Town 7945, South Africa
[12] Center of Astrophysics and Planetary Sciences, Racah Institute of Physics, The Hebrew University of Jerusalem, Jerusalem 91904, Israel
[13] National Optical Astronomy Observatory, 950 N. Cherry Avenue, Tucson, AZ 85721, USA
[14] Department of Astronomy, University of Texas, Austin, TX 78712, USA
[15] Department of Physics & Astronomy, Rutgers University, Piscataway, NJ 08854, USA
[16] University of California Observatories/Lick Observatory, University of California, Santa Cruz, CA 95064, USA
[17] Department of Physics and Astronomy, University of Kentucky, Lexington, KY 40506, USA
[18] Kavli Institute for Particle Astrophysics and Cosmology, Stanford University, Stanford, CA 94305, USA
[19] Department of Physics, University of Missouri-Kansas City, 5110 Rockhill Road, Kansas City, MO 64110, USA
[20] Department of Physics and Astronomy, University of California, Riverside, CA 92521, USA
[21] Carnegie Observatories, Pasadena, CA 91101, USA
[22] Institute for Astronomy, University of Hawaii at Manoa, Honolulu, HI 96822-1897, USA
[23] Canada-France-Hawaii Telescope Corporation, Kamuela, HI 96743-8432, USA
[24] Department of Physics & Astronomy, The Johns Hopkins University, Baltimore, MD 21218, USA
[25] Department of Astronomy, Yale University, New Haven, CT 06520, USA
[26] Steward Observatory, University of Arizona, Tucson, AZ 85721, USA
[27] Harvard-Smithsonian Center for Astrophysics, Cambridge, MA 02138, USA
Received 2014 July 20; accepted 2014 December 10; published 2015 April 9

ABSTRACT

Galaxies with stellar masses near M^* contain the majority of stellar mass in the universe, and are therefore of special interest in the study of galaxy evolution. The Milky Way (MW) and Andromeda (M31) have present-day stellar masses near M^*, at $5 \times 10^{10}\ M_\odot$ (defined here to be MW-mass) and $10^{11}\ M_\odot$ (defined to be M31-mass). We study the typical progenitors of these galaxies using the FourStar Galaxy Evolution Survey (ZFOURGE). ZFOURGE is a deep medium-band near-IR imaging survey, which is sensitive to the progenitors of these galaxies out to $z \sim 3$. We use abundance-matching techniques to identify the main progenitors of these galaxies at higher redshifts. We measure the evolution in the stellar mass, rest-frame colors, morphologies, far-IR luminosities, and star formation rates, combining our deep multiwavelength imaging with near-IR *Hubble Space Telescope* imaging from Cosmic Near-IR Deep Extragalactic Legacy Survey (CANDELS), and *Spitzer* and *Herschel* far-IR imaging from Great Observatories Origins Deep Survey-Herschel and CANDELS-Herschel. The typical MW-mass and M31-mass progenitors passed through the same evolution stages, evolving from blue, star-forming disk galaxies at the earliest stages to redder dust-obscured IR-luminous galaxies in intermediate stages and to red, more quiescent galaxies at their latest stages. The progenitors of the MW-mass galaxies reached each evolutionary stage at later times (lower redshifts) and with stellar masses that are a factor of two to three lower than the progenitors of the M31-mass galaxies. The process driving this evolution, including the suppression of star formation in present-day M^* galaxies, requires an evolving stellar-mass/halo-mass ratio and/or evolving halo-mass threshold for quiescent galaxies. The effective size and SFRs imply that the baryonic cold-gas fractions drop as galaxies evolve from high redshift to $z \sim 0$ and are strongly anticorrelated with an increase in the Sérsic index. Therefore, the growth of galaxy bulges in M^* galaxies corresponds to a rapid decline in the galaxy gas fractions and/or a decrease in the star formation efficiency.

Key words: galaxies: evolution – galaxies: high-redshift – galaxies: structure

1. INTRODUCTION

Studying the formation of galaxies with stellar masses like the Milky Way (MW) and Andromeda (M31) provides insight into the formation of large galaxies and the most common

* This paper contains data gathered with the 6.5 m Magellan Telescopes located at Las Campanas Observatory, Chile.
[28] Mitchell Astronomy Fellow.
[29] Australian Research Council Super Science Fellow.

locations of stars in the present universe. Galaxies with these masses constitute the majority of the bright galaxy population in the local universe: by number they represent 70% of the intermediate-mass galaxy population (ranging from 3×10^{10} to $3 \times 10^{11}\ M_{\odot}$), and they contain more than two-thirds of the present-day stellar-mass density when integrated over the entire mass function (e.g., Hammer et al. 2007). Despite the fact that these galaxies are so ubiquitous and common, our knowledge of the formation of these galaxies, such as the MW, is still largely incomplete (Rix & Bovy 2013).

Both the MW and M31 have stellar masses very near the present-day values of M^*, the characteristic stellar mass of the galaxy stellar-mass function, which is described by the well-known Schechter function (see, e.g., Bell et al. 2003; Baldry et al. 2008; Ilbert et al. 2013; Moustakas et al. 2013; Muzzin et al. 2013; Tomczak et al. 2014, and references therein),

$$\phi(M_*)\,dM_* = \phi^* \left(\frac{M_*}{M^*}\right)^{\alpha} \exp(-M_*/M^*)\frac{dM_*}{M^*}. \qquad (1)$$

M^* is a fundamental parameter and corresponds to the point where the stellar-mass function transitions from a power law in stellar mass to an exponentially declining cutoff.[30] As illustrated in Figure 1, M^* sits near the peak of the stellar-mass-distribution function (the product of the stellar-mass function and the stellar mass): M^* is the "mode" of the stellar-mass-density distribution function. Therefore a typical star (such as the Sun) most commonly resides in galaxies of this stellar mass at present (van Dokkum et al. 2013).[31] By studying the evolution of present-day M^* galaxies, we are able to learn about the most common sites of stars in the present-day universe, including the formation of the MW and M31.

The complex evolution of M^* galaxies has been the focus of galaxy formation models within cosmological simulations, which include the properties of dark matter, gas accretion, and feedback (e.g., Bournaud et al. 2007a; Elmegreen et al. 2008; Agertz et al. 2009; Dekel et al. 2009; Martig et al. 2009; Martig & Bournaud 2010). These studies have included the effects of cold gas flows, star-forming clump formation and migration, and violent disk instabilities on bulge formation (Ceverino et al. 2010, 2012; Sales et al. 2012; Zavala et al. 2012; Dekel et al. 2009, 2013; Dekel & Burkert 2014). These models make predictions for the relation between stellar-mass growth, structural evolution, and the evolution of the star formation rate (SFR), gas accretion rate, and gas fraction for galaxies with masses of the MW and M31.

Comparing the predictions from models of M^* galaxy formation to data has been hindered by observational limitations. The models predict that the progenitors of these galaxies should have stellar masses of $\lesssim 10^{10}\ M_{\odot}$ at $z \gtrsim 2$ (e.g., de Rossi et al. 2009; Moster et al. 2013; Behroozi et al. 2013a), and surveys typically with the depth required to be complete for this stellar mass have very small fields that lack the cosmic volume to trace the progenitors of these galaxies across cosmic time in a homogeneous data set (e.g., to be complete for galaxies to this limiting stellar mass at this redshift requires typically $K_{\rm AB} \gtrsim 24$ mag; see, for example, Bassett et al. 2013). Furthermore, although simulations track the formation of individual MW-like galaxies over long baselines in time, this is clearly not possible in observational surveys. Rather, to make empirical constraints requires that we identify galaxies at high redshift that are statistically similar to the progenitors of nearby galaxies observed over a range of redshift.

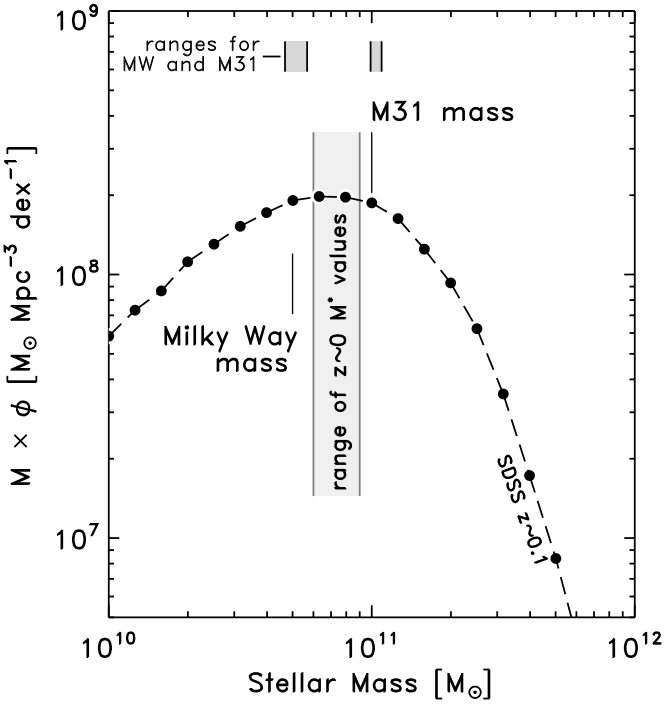

Figure 1. Stellar-mass density distribution derived from the product of stellar mass and the stellar-mass function at $z \sim 0.1$ (Moustakas et al. 2013, see also van Dokkum et al. 2013). These distributions peak around M^*, the characteristic mass of the Schechter function, and the large shaded swath indicates the range of low-redshift M^* values in the literature. Our adopted values for the mass of MW-mass galaxies (stellar mass of $5 \times 10^{10}\ M_{\odot}$) and M31-mass galaxies ($10^{11}\ M_{\odot}$) are indicated in the figure. These are consistent with measurements of the MW and M31 proper, where the smaller shaded regions near top of the figure show the values for the MW and M31 from Mutch et al. (2011). Our adopted values for the MW-mass and M31-mass galaxies span the full range of M^*, allowing us to study the range of galaxies with masses near the mode of the stellar-mass density distribution, and this includes possible formation histories of our own Galaxy.

Recent surveys, using very deep near-IR imaging have begun to study the evolution of present-day galaxies such as the MW. Using data from the 3D-HST and Cosmic Near-IR Deep Extragalactic Legacy Survey (CANDELS) surveys, van Dokkum et al. (2013) studied the assembly history and evolution of structural properties of galaxies with a present-day mass of an MW-sized galaxy (assuming $M_* \simeq 5 \times 10^{10}\ M_{\odot}$) by assuming the main progenitors of these galaxies have constant (comoving) number density at higher redshift. They found that ~90% of the stellar mass in these galaxies has been built since $z \sim 2.5$ without any significant merging. Patel et al. (2013a) focused on star-forming progenitors of galaxies with a present-day stellar mass of $\simeq 3 \times 10^{10}\ M_{\odot}$, based on the evolution of galaxies along the star-forming "main sequence" (e.g., Noeske et al. 2007; Karim et al. 2011; Leitner 2012). Both the studies of van Dokkum et al. and Patel et al. found a peak SFR $\simeq$ 10–15 $M_{\odot}\ {\rm yr}^{-1}$ at $z \sim$ 1–2

[30] Although there is evidence that the galactic stellar-mass function is better represented as a double-Schechter function these double-Schechter functions are typically consistent with a single M^* value, at least for $z < 2$, e.g., Baldry et al. (2008) and Tomczak et al. (2014).

[31] At any redshift the most common location of stars will be in galaxies around the value $M^*(z)$. Because $M^*(z)$ does not evolve strongly with redshift (see, e.g., Ilbert et al. 2013; Muzzin et al. 2013; Tomczak et al. 2014), it is only at present ($z = 0$) that galaxies with masses like the MW and M31 are the most common locations of stars. As we discuss in this paper, the progenitors of MW-mass and M31-mass galaxies are lower than M^* at earlier times (higher redshift), and therefore the progenitors of the MW-mass and M31-mass galaxies are *not* the most common locations of stars at earlier epochs.

for these galaxies, where most of this stellar-mass growth occurred at nearly the same rate at all radii with no evidence for inside-out growth, at least for progenitors at $z > 0.6$.

However, it remains unclear how this evolution proceeded, and what physical processes regulated it. Clearly, if star formation dominated the formation of M^* galaxies as suggested by van Dokkum et al. (2013) and Patel et al. (2013a), then their growth was heavily dependent on the evolution of their cold gas supply and their gas-accretion histories (the SFR is expected to track the gas accretion history; see, e.g., Agertz et al. 2009; Dekel et al. 2013). Therefore, understanding the evolution of the galaxies' gas is paramount. Clearly, the processes driving galaxy formation and assembly depend on galaxy mass (e.g., Moster et al. 2013). Because these processes are complex, the assembly histories of the progenitors of present-day M^*-mass galaxies should have a large variation that depends on the mass of the galaxies' main progenitors (e.g., Behroozi et al. 2013a). Therefore, to study how the formation of M^* galaxies proceeded, it is important to consider how the physical properties of these galaxies evolved as a function of stellar mass and redshift.

Here we use data from a combined set of deep surveys to study the evolution of progenitors of M^* galaxies. The combined data sets here include data from the FourStar Galaxy Evolution (ZFOURGE) survey, the CANDELS, including *Spitzer* and *Herschel* imaging from CANDELS-Herschel (CANDELS-H) and the Great Observatories Origins Deep Survey-Herschel (GOODS-H).

The outline for this paper is as follows. Section 2 discusses the properties of present-day M^* galaxies and how they relate to the MW and M31. Section 3 describes the ZFOURGE, CANDELS *Hubble Space Telescope* (*HST*), *Spitzer*, and *Herschel* data sets, and it discusses the derivation of physical properties such as photometric redshifts, stellar masses, rest-frame colors, sizes, and Sérsic indices. Section 4 discusses the selection of M^* galaxy progenitors (including the progenitors of MW-mass and M31-mass galaxies), incorporating the expected galaxy growth from abundance matching methods. Section 5 discusses the color of the M^* galaxy progenitors, and Section 6 discusses the evolution of the galaxy morphologies. Section 7 describes the stacked far-IR data from the M^* galaxy progenitor samples, and it discusses the evolution in galaxy IR luminosities, SFRs, and implied gas fractions. Section 8 discusses constraints on the growth of M^* galaxy progenitors, and shows how the combination of these independent data sets tells a consistent story for the evolution of M^* galaxy progenitors. Section 9 summarizes our conclusions.

All magnitudes here are relative to the AB system (Oke & Gunn 1983). We denote photometric magnitudes measured in the *HST*/WFC3 F125W and F160W passbands as J_{125} and H_{160}, respectively. Throughout, we use $*$ in the subscript, M_*, to denote derived stellar masses of individual galaxies. We use $*$ in the superscript, M^*, to denote the characteristic mass of the stellar-mass function. For all derived quantities, where applicable we assume a cosmology with $\Omega_m = 0.27$, $\Omega_\Lambda = 0.73$, and $H_0 = 70.4$ km s^{-1} Mpc^{-1}, consistent with the *WMAP* seven-year data (Komatsu et al. 2011).

2. ON THE PROPERTIES OF M^* GALAXIES: THE MW AND M31

This paper focuses on the evolution of the main progenitors of M^* galaxies in two bins of stellar mass. We define "MW-mass" and the "M31-mass" galaxies to be those galaxies with present-day ($z = 0$) stellar masses near $M_* = 5 \times 10^{10}\ M_\odot$ and $M_* = 10^{11}\ M_\odot$, respectively. These stellar masses are consistent with the range for the MW and M31 currently published in the literature (see Mutch et al. 2011, and references therein; and also McMillan 2011; van Dokkum et al. 2013; Licquia & Newman 2014), based on the modeling of the MW and M31 luminosities with M/L ratios consistent with that of a Chabrier 2003 initial mass function (IMF; see Flynn et al. 2006; Geehan et al. 2006). (However, see the recent study of Gibbons et al. 2014, who derived a much lower mass for the MW compared to other work.) As illustrated in Figure 1, the adopted masses for the MW and M31 span the range in the literature for present-day ($z < 0.05$) values of M^*, which range from 6×10^{10} (Baldry et al. 2008) to 9×10^{10} (Bell et al. 2003; Marchesini et al. 2009; accounting for differences in the Hubble parameter and IMF). Therefore, our investigation probes the evolution of MW-mass and M31-mass progenitors. These bracket the observed range of M^* galaxies, and allows us to compare the empirical evolution for such galaxies that at present differ in stellar mass by a factor of two.

Although throughout this paper we discuss the evolution of M^* galaxies in subsamples of MW-mass and M31-mass galaxies, the MW and M31 themselves may be outliers. Indeed, there is growing evidence that neither the MW nor M31 themselves are "typical" of the galaxy population at these masses. Mutch et al. (2011) presented a comparison of the MW and M31 galaxies to other galaxies with similar stellar masses selected from the Sloan Digital Sky Survey (SDSS). They concluded that both the MW and M31 have bluer optical colors at fixed stellar mass compared to galaxies matched in stellar mass and morphology in SDSS: both the MW and M31 reside in the "green valley" of the galaxy color–mass distribution. Mutch et al. concluded that the MW and M31 are in the process of transitioning their global properties from star-forming to more quiescent phases of galaxy evolution. In contrast, the "typical" M^* galaxy is already a red-sequence galaxy in SDSS.

A perusal of M31- and MW-mass galaxies in the SDSS is consistent with this conclusion. Figures 2 and 3 show montages of M31-mass and MW-mass galaxies randomly selected from SDSS DR7 with $0.02 < z < 0.03$ and stellar mass $10.9 < \log M_*/M_\odot < 11.1$, and $10.6 < \log M_*/M_\odot < 10.8$, within 0.1 dex of our adopted values for M31 and the MW, respectively (using stellar masses for SDSS DR7 derived from the MPA-JHU value-enhanced catalog[32]; Brinchmann et al. 2004). The montages in Figures 2 and 3 show that the typical M31-mass and MW-mass galaxies are spheroidal, or reddened, bulge-dominated disks. Qualitatively, many of these galaxies appear to have a more early type of morphology compared to both the MW and M31, except for a fraction of cases where bluer, spiral structures are apparent.

The preponderance of early-type morphologies among the MW-mass galaxies is at odds with observations of the MW. For example, Mutch et al. (2011) argue that the MW is an Sb/c Hubble type. The mass of the MW's central supermassive black hole (SMBH) is low compared to either its dark-matter halo, or its perceived bulge mass. This may be mitigated if the MW has only a pseudo-bulge (where SMBH mass is known to correlate with "classical" bulge mass; Kormendy et al. 2011), and these observations reinforce the idea that the morphology of the MW is of a later type than the typical MW-mass galaxy in SDSS.

[32] http://home.strw.leidenuniv.nl/~jarle/SDSS/

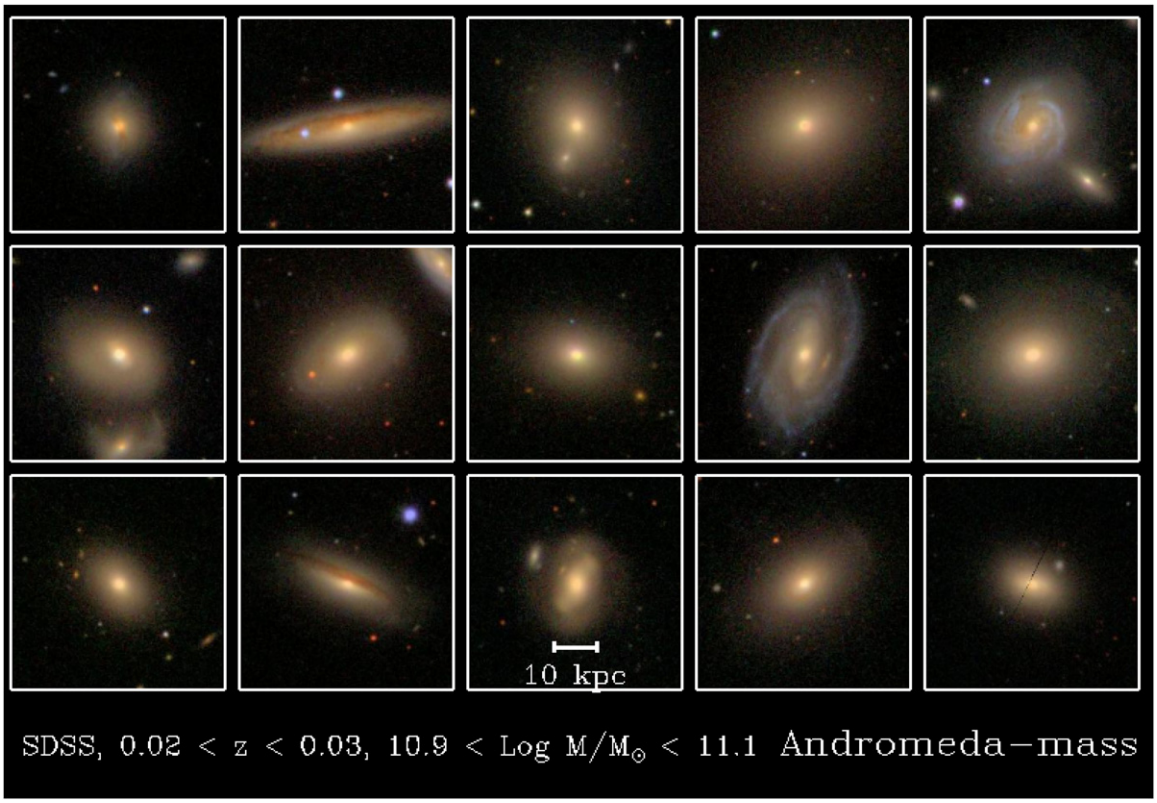

Figure 2. Montage of galaxies selected randomly from SDSS with $0.02 < z < 0.03$ and stellar mass $10.9 < \log M_*/M_\odot < 11.1$: these are present-day M31-mass galaxies using our choice of stellar mass. The images are SDSS gri-band composites. The montage shows that at $z \sim 0$ these galaxies are dominantly spheroidal and early type. Although some examples of disk galaxies with spiral structures are evident, these structures are not the norm for M31-mass galaxies.

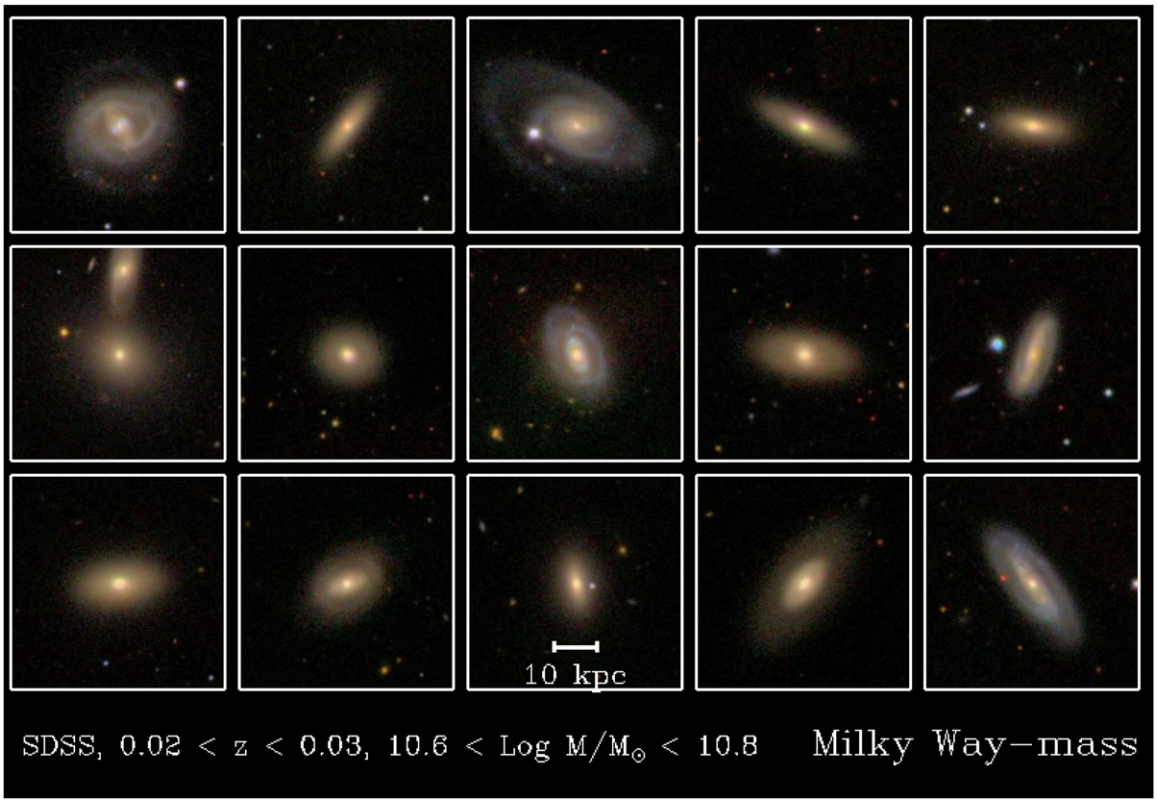

Figure 3. Montage of galaxies selected randomly from SDSS with $0.02 < z < 0.03$ and stellar mass $10.6 < \log M_*/M_\odot < 10.8$: these are the present-day MW-mass galaxies using our choice of stellar mass. The images are SDSS gri-band composites. As with Figure 2, this montage shows that galaxies at present with these stellar masses are dominantly spheroidal and early type, although some examples of disk galaxies with blue (star-forming) spiral structures are present.

Therefore, while both M31 and the MW are examples of M^* galaxies, they are not themselves the most representative of the M^* population. The results that we derive in this paper pertain to the median evolution of galaxies with present-day masses $5 \times 10^{10}\,M_\odot$ and $10^{11}\,M_\odot$. While this provides insight into the formation and assembly history of the MW and M31 themselves, it may be that these do not necessarily pertain to the exact history for either galaxy.

3. ZFOURGE AND ANCILLARY DATA SETS

The ZFOURGE survey (I. Labbé et al. 2014, in preparation) is a deep medium-band near-IR survey using the FourStar instrument (Persson et al. 2013) mounted on the Magellan/Baade Telescope. The main ZFOURGE survey obtained very deep near-IR imaging in five adjacent medium-band filters (J_1, J_2, J_3, H_s, H_l) and a standard K_s filter. The FourStar J_1 filter provides similar coverage as the now more commonly used Y-band filter on near-IR imagers, and the J_2J_3 and H_sH_l filter pairs divide the J-band and H-band near-IR windows (see, e.g., Tilvi et al. 2013). These medium-band filters are very similar to those used by the NEWFIRM Medium-Band survey (van Dokkum et al. 2009; Whitaker et al. 2011), with small differences (particularly the central wavelength of the J_2 filter; see Tilvi et al. 2013). The filters provide $R \sim 10$ "spectroscopy" of the Balmer-break as it moves through these bands at $1 < z < 4$. As a result, the bands provide accurate photometric redshifts $\sigma(z)/(1+z) \approx 1\%$–$2\%$ (e.g., van Dokkum et al. 2009; Whitaker et al. 2011; Spitler et al. 2012; Kawinwanichakij et al. 2014; T. Yuan et al., in preparation).

Here, we use the main ZFOURGE survey, which imaged three $11' \times 11'$ fields, widely separated on the sky: the CDF-S, COSMOS, and UKIDSS Ultra Deep Survey (UDS) fields. The ZFOURGE pointings overlap with the deepest portions of the CANDELS *HST* imaging, and deep *Spitzer* and *Herschel* imaging, described below. Our FourStar images achieve depths of $K_s = 24.80$, 25.16, 24.63 AB mag, in each field, respectively (5σ), measured in $0\farcs6$ diameter apertures, corrected to total apertures based on the curve of growth for point sources. In addition, for the UDS field we use a detection image that is the sum of our FourStar K_s image and the K_s image from the UKIDSS DR8.[33] The total depth of this image is $K_s = 25.2$ AB mag measured from the same aperture as above. The depths in the other FourStar bands are designed to match the colors of red, passive galaxies at $z > 1$, reaching $J_1 \approx K_s + 1$ mag. The data quality of the FourStar images is excellent, with the FWHM $\simeq$ 0.5–$0\farcs6$ for the point-spread function (PSF) for the stacked FourStar images (Tilvi et al. 2013).

We combined the FourStar near-IR images with existing ancillary ground-based imaging (spanning U through z bands), the CANDELS *HST*/Advanced Camera for Surveys (ACS) and WFC3 imaging (Grogin et al. 2011; Koekemoer et al. 2011), and *Spitzer*/IRAC imaging to generate multiwavelength catalogs spanning 0.3–8 μm (the exact bands available depend on the field; see Tomczak et al. 2014, and the acquisition, data reduction, and description of the multiwavelength catalogs will appear in C. Straatman et al. 2014, in preparation).[34] For each field, the ground-based and *HST* images are convolved to match the seeing in the image with the worst image quality (largest FWHM). Photometry is measured in $1\farcs2$ diameter circular apertures, and an aperture correction applied using the K_s data for each source. Typically, the relative flux for point sources between bands is matched to better than 2% for circular apertures with radii larger than $0\farcs47$. The IRAC 3.6, 4.5, 6.8, and 8.0 μm data were matched to the optical/near-IR catalogs using the procedure described in Labbé et al. (2006, 2010).

3.1. Photometric Redshifts, Stellar Masses, and Rest-frame Colors

Photometric redshifts were derived using the full multiwavelength catalogs spanning 0.3–8 μm with EAZY (Brammer et al. 2008). EAZY reports small uncertainties on the photometric redshifts for the ZFOURGE samples. For the M^*-progenitor subsamples used here, the average 68% uncertainties on the photometric redshifts range from $\sigma(z)/(1+z) = 0.013$–0.020, (see also the discussion in Kawinwanichakij et al. 2014). Rest-frame colors are derived using InterRest (Taylor et al. 2009) using the EAZY photometric redshifts. We focus on the $U-V$ and $V-J$ rest-frame colors of the M^* progenitor subsamples. We estimated uncertainties on these rest-frame colors, remeasuring the colors in a Monte Carlo simulation, perturbing the fluxes of each object 1000 times and taking the inter-68th percentile range as the uncertainty. The average uncertainties on these rest-frame colors are $\sigma(U-V) = 0.06$–0.12 mag and $\sigma(V-J) = 0.10$–0.19 mag for the M^* progenitors over the redshift range $z \sim 0.5$–3.

Stellar masses were derived by fitting Bruzual & Charlot (2003) stellar population synthesis models with FAST (Kriek et al. 2009) using a Chabrier (2003) IMF, solar metallicity, and using exponentially declining star-forming histories ($\Psi \sim \exp(-t/\tau)$), where the age ranges from $\log t/\mathrm{yr} = 7.5$–10.1 in steps of 0.1 dex and the e-folding timescale ranges from $\log \tau/\mathrm{yr} = 7.0$–11.0 in steps of 0.2 dex. The effects of dust attenuation were included using the prescription from Calzetti et al. (2000) ranging from $A_V = 0$–4.0 mag in steps of 0.1 mag. Adopting different extinction laws can affect the stellar masses at the $\sim$0.2–0.3 dex level (e.g., Papovich et al. 2001; Marchesini et al. 2009; Tilvi et al. 2013). While we expect the metallicity of the M^* progenitors to evolve over the redshift range studied here, assuming different metallicities in the fitting of the spectral-energy distributions has only a minor impact on stellar masses (e.g., Papovich et al. 2001; Gallazzi & Bell 2009; Marchesini et al. 2009). Assumptions about the star formation histories and different fitting methods can introduce systematic uncertainties at the $\simeq$0.2 dex level (see, e.g., Maraston et al. 2010; Lee et al. 2011; Papovich et al. 2011; Pacifici et al. 2015). The typical statistical uncertainities on the stellar masses from FAST for the M^* progenitors are formally 0.10–0.14 dex depending on mass and redshift. Therefore, we expect the combined uncertainties on the stellar masses (statistical and systematic) to be $<$0.2–0.3 dex level (factor of two), dominated by systematics.

3.2. Stellar-mass Completeness

We estimated the completeness in the current ZFOURGE images and catalogs, and in our samples of M^* galaxies (defined in Section 5) in two ways. First, we compared the completeness in stellar mass in the ZFOURGE catalogs to the catalogs from 3D-HST (Skelton et al. 2014, see below), which provide an empirical test of our catalogs to $z \lesssim 3$ where 3D-HST achieves deeper stellar-mass completeness. Second, we performed simulations where we inserted fake point sources

[33] http://www.nottingham.ac.uk/astronomy/UDS/
[34] See also http://zfourge.tamu.edu

in the K_s-detection image for each of the three ZFOURGE fields. We allow the sources to have magnitudes chosen from a wide distribution, and we allow the sources to be located anywhere in the detection image. In this way random objects may fall within the isophote of real objects in the image, and therefore our completeness simulations include the effects from blended objects. We measure the 80% completeness limit to be the magnitude where we recover 80% of the fake sources using the same detection parameters as for the real catalog. For the ZFOURGE CDF-S, COSMOS, and UDS catalogs the 80% completeness limits are $K_s = 24.53$, 24.74, and 25.07 AB mag, respectively (the 90% completeness limits are approximately 0.2 mag shallower in each field). From our simulations, we also estimate that blended objects account for 5% of this incompleteness. For the remainder of this work, we consider samples where the data are formally 80% complete.

The 3D-HST catalogs provide an estimate of our stellar-mass completeness for $z < 3$ because at these redshifts the (deeper, H_{160}-band selected) 3D-HST catalog achieves a lower stellar-mass limit than our (shallower, K_s-band-selected) ZFOURGE catalog. We matched sources in ZFOURGE to 3D-HST in the regions where they overlap, and we computed the completeness as the fraction of sources in 3D-HST detected in ZFOURGE in bins of stellar mass and redshift. The 80% completeness in stellar mass is $\log M/M_\odot = 8.8$, 9.2, 9.4, 9.5, and 9.8 dex in bins of $1 < z < 1.5$, $1.5 < z < 2$, $2 < z < 2.5$, $2.25 < z < 2.75$, and $2.5 < z < 3$, respectively (where the penultimate bin is about the same redshift range as the highest-redshift bin for our MW progenitor subsample). This test also accounts for completeness effects as a result of galaxy properties themselves, including blending between sources that are resolved in the *HST* catalog, but blended at the FourStar resolution, the intrinsic colors of galaxies (including possible dust-obscured, low-mass galaxies), and for the fact that the galaxies in our samples are not point sources.

Based on the comparison to 3D-HST and the point-source simulations, the MW-mass progenitors are >90% complete for $z < 2.2$. At this redshift, the MW-mass progenitors are already mostly star-forming, with blue colors and low dust obscuration (based on their $L_{\rm IR}/L_{\rm UV}$ ratios, see Sections 5 and 7, below). Such blue objects have lower M/L ratios, and are complete to lower stellar mass than the completeness derived for the K_s-band limit. Because the MW-mass progenitors are already blue with no indication of a significant population of very dust-reddened or quiescent progenitors, it seems unlikely that such a population would suddenly be part of the MW-mass progenitor population at higher redshift at lower stellar masses. Therefore, we expect the MW-mass progenitors to be reasonably (80%) complete in their highest redshift bin, $2.2 < z < 2.8$, and this is consistent with the comparison to 3D-HST.

The M31-mass progenitors are >90% complete for $z < 2.8$. The formal 80% completeness stellar-mass limit (from our simulations and the K_s-band limit) is moving through the highest-redshift bin for the M31-mass progenitors, $2.8 < z < 3.5$, but we expect higher completeness because the populations have relatively blue colors at lower redshifts, $z < 2.8$. Nevertheless, the stellar-mass completeness values are only estimates, and these would be biased if there existed a significant, undetected population of low-mass, dusty, or quiescent red galaxies. Any conclusions about the M^* galaxies in their highest-redshift bins could be biased if these samples are missing a hypothetical population of redder galaxies than those counted in our simulations.

3.3. HST Imaging

The three ZFOURGE fields (COSMOS, CDF-S, UDS) overlap with the CANDELS *HST* imaging with WFC3 using the F125W and F160W passbands. The *HST* data provide higher angular resolution imaging (FWHM $\simeq 0\farcs2$; see Koekemoer et al. 2011) compared to any of the ground-based data sets, and this allows us to resolve structures down to ~1 kpc. We make use of the galaxy structural properties (effective sizes and Sérsic indices) measured with the CANDELS *HST* imaging with WFC3 published by van der Wel et al. (2012). Throughout this work we focus on the sizes and Sérsic indices measured in the F160W band as this allows measurements in the rest-frame 4000 Å (approximately the *B* band) out to $z \sim 3$. In addition, the CANDELS coverage of the CDF-S field includes F105W imaging, as well as the ACS imaging from 0.4 to 1 μm in the F435W, F606W, F775W, and F850LP bandpasses from GOODS (Giavalisco et al. 2004). At lower redshifts, the F160W band probes light from longer rest-frame wavelengths. However, our tests using data from the WFC3 F105W passband in the CDF-S show that the differences in the structural parameters are minor, and that none of our conclusions would be affected.

We matched the sources in the ZFOURGE catalogs to those in van der Wel et al. (2012) using a matching radius of $0\farcs5$. We then adopt the effective semimajor axis and Sérsic index for each source from the van der Wel et al. catalog. Here, the effective sizes we report are the circularized effective radius, $r_{\rm eff} = \sqrt{ab} = a_{\rm eff}\sqrt{q}$, where $a_{\rm eff}$ is the effective semimajor axis measured in van der Wel et al., and $q = b/a$ is the ratio of the semiminor to semimajor axes.

3.4. Spitzer and Herschel Far-IR Imaging

The ZFOURGE fields cover areas with imaging from *Spitzer*/MIPS and *Herschel*/PACS. We use the deepest of these data to measure the mid-IR and far-IR emission for galaxy populations selected from ZFOURGE. In practice, we are interested here in the average IR emission from galaxies in our samples. To ensure we are not biased by the subset of galaxies detected in the mid-IR and far-IR data, we will stack the IR data at the locations of the galaxies in our samples to produce average flux density measurements (see Section 7.1).

For the ZFOURGE CDF-S field, we used *Spitzer*/MIPS 24 μm imaging from the GOODS *Spitzer* Legacy program (PI: M. Dickinson; see also Magnelli et al. 2011). For the *Herschel*/PACS 100 and 160 μm imaging, we used the data taken by the GOODS-H (a *Herschel* Key Project; Elbaz et al. 2011).

For the COSMOS field, we used MIPS 24 μm imaging from the SCOSMOS *Spitzer* Legacy program (PI: D. Sanders).[35] We also used deep PACS 100 and 160 μm data from CANDELS-H (H. Inami et al., in preparation), reduced in the same way as GOODS-H.

For the UDS field, we used the MIPS 24 μm imaging from SpUDS *Spitzer* Legacy program (PI: J. Dunlop),[36] combined with deep data taken with PACS at 100 and 160 μm also as part of CANDELS-H.

4. SELECTING THE PROGENITORS OF M^* GALAXIES

There is a growing body of work in the literature that select the progenitors of galaxies at higher redshifts (earlier cosmic epochs) by requiring that they have the same co-moving,

[35] http://irsa.ipac.caltech.edu/data/SPITZER/S-COSMOS
[36] http://irsa.ipac.caltech.edu/data/SPITZER/SpUDS

cumulative number density (Brown et al. 2007, 2008; Cool et al. 2008; van Dokkum et al. 2010, 2013; Papovich et al. 2011; Bezanson et al. 2011; Brammer et al. 2011; Fumagalli et al. 2012; Conselice et al. 2013; Leja et al. 2013; Muzzin et al. 2013; Patel et al. 2013b; Lundgren et al. 2014; Tal et al. 2014; Marchesini et al. 2014). This method is an approximation, as it neglects variations (scatter) in mass growth, including effects of galaxy mergers on the mass-rank order of galaxies. Leja et al. (2013) compared the selection of progenitors using constant number density to other means using a mock catalog from the Millennium simulation. They showed that selecting galaxies based on constant number density reproduces the stellar mass of progenitors, but with uncertainties of 0.15 dex from $z = 3$ to 0. Behroozi et al. (2013a) recently discussed how the selection at constant number density ignores scatter in mass accretion histories and mergers, which can lead to errors in the mass evolution of galaxy progenitors on the order of $d(\log M_*)/dz = 0.16$ dex (i.e., factor of ≈40% per unit redshift). This error is exacerbated for galaxies with lower $z = 0$ stellar masses (larger number densities).

Here, we have used results of a multi-epoch abundance matching (MEAM) method (Moster et al. 2013) to identify the main progenitors of present-day M^* galaxies at higher redshifts. Moster et al. derived a redshift-dependent parameterization of the stellar-mass to halo-mass relation, whereby they populate dark-matter halos and subhalos in the Millennium simulations with galaxies that follow a distribution of stellar mass, such that the evolution of observed stellar mass functions are reproduced simultaneously. Behroozi et al. (2013b) used a similar method (also called "stellar-halo-mass abundance matching") applied to the independent Bolshoi simulation to show that this reproduces both the stellar-mass function evolution and the star formation history over a large range of galaxy mass and redshift ($0 < z < 8$). Because the abundance-matching methods of Moster et al. and Behroozi et al. track the evolution of galaxies with their dark-matter halo evolution, they naturally correct for variations in galaxy mass growth and galaxy mergers compared to techniques that select progenitors at constant number density. Nevertheless, as Figure 4 shows, all methods produce very similar mass evolution (see also Leja et al. 2013).

We derive the stellar-mass evolution of galaxy progenitors using the results of Moster et al. (2013), who provided fitting functions for the star formation history and mass accretion history for galaxies of arbitrary present-day stellar mass. We integrated the Moster et al. (2013) fitting functions with respect to time, accounting for mass losses from stellar evolution (see Moster et al. 2013, their Equation (16)) to derive the conditional stellar-mass evolution of galaxies. Figure 4 shows the stellar-mass evolution of present-day galaxies with $5 \times 10^{10}\,M_\odot$ (MW-mass galaxies) and $10^{11}\,M_\odot$ (M31-mass galaxies).[37] This growth is more rapid at $z > 1$, with $\log M_* \propto -1.1\Delta z$, which can be compared to the predicted halo growth based on simple theoretical grounds, where $\log M_h \propto -0.8\Delta z$ (Dekel et al. 2013; valid at $z > 1$). This is expected as at these redshifts the halo mass corresponding to the peak value in M_*/M_h (related to the star formation efficiency) decreases with redshift (e.g., Behroozi et al. 2010, 2013b).

[37] The stellar-mass evolution we derive via integrating the star formation and accretion histories matches the direct results from Moster et al. at $z \sim 0$, but produces masses $\lesssim$0.15 dex lower at $z = 2$ (B. Moster 2013, private communication). These are both within the plausible range of mass-growth histories in Moster et al. (2013), and so both are equally consistent.

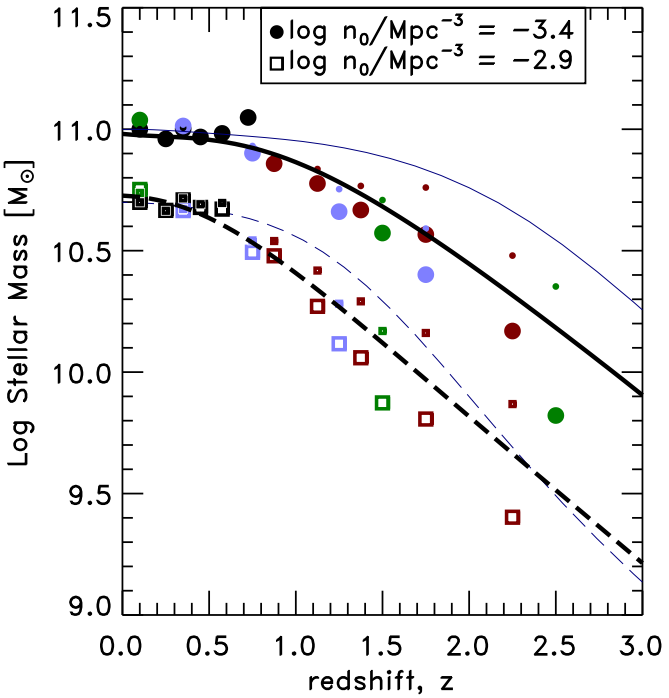

Figure 4. Stellar-mass evolution of galaxies of M31-mass (present-day stellar mass $10^{11}\,M_\odot$) and MW-mass (stellar mass $5 \times 10^{10}\,M_\odot$) progenitors as a function of redshift. The data points show the stellar-mass evolution of galaxies selected by their number density for present-day ($z = 0$) values $\log(n_0/\mathrm{Mpc}^{-3}) = -2.9$ for the MW-mass (open boxes) and $\log(n_0/\mathrm{Mpc}^{-3}) = -3.4$ for the M31-mass (filled circles) progenitors. The different colors represent values for different literature mass functions (black: Moustakas et al. 2013; blue: Muzzin et al. 2013; green: Marchesini et al. 2009; red: Tomczak et al. 2014), where we show points only at redshifts where the mass functions are complete. The small data points show the evolution for constant co-moving number density, derived by integrating stellar-mass functions down to the same number density at each redshift. The large data points show the mass evolution for an evolving number density from Behroozi et al. (2013a). The thick solid and dashed curves show the stellar-mass evolution from the abundance-matching model of Moster et al. (2013) for galaxies with $M_* = 10^{11}$ and $M_* = 5 \times 10^{10}\,M_\odot$, respectively, at $z = 0$. Galaxies with these stellar masses at $z = 0$ have halo masses of $M_h = 10^{13}$ and $2.5 \times 10^{12}\,M_\odot$, respectively in this model. The thin solid and dashed lines show the evolution for galaxies with the same present-day stellar masses based on modeling their median star formation histories (Behroozi et al. 2013b). Here, we use the stellar-mass evolution from Moster et al. model to select progenitors of MW-mass and M31-mass galaxies.

Figure 4 shows the expected stellar-mass evolution at constant and evolving number density (using the prescription of Behroozi et al. 2013a). Using the stellar-mass function at $z \sim 0.1$ from SDSS (Moustakas et al. 2013) we find that galaxies with present-day stellar masses of $5 \times 10^{10}\,M_\odot$ and $10^{11}\,M_\odot$ have number densities $\log(n/\mathrm{Mpc}^{-3}) = -2.9$ and -3.4, respectively, where rarer objects with lower number density have higher mass. We then integrate the literature mass functions (Moustakas et al. 2013; Muzzin et al. 2013; Marchesini et al. 2009; Tomczak et al. 2014) to the appropriate number density at different redshifts down to the stellar mass such that $n(>M_*) =$ constant (for constant number density) or to the evolving number density predicted by Behroozi et al. (2013a). We only include data points in Figure 4 where the mass functions are complete.

A comparison of the data points and curves in Figure 4 shows that for M^*-mass galaxies the stellar-mass evolution derived using the Moster et al. (2013) abundance matching is mostly consistent to that measured using samples at fixed number density. There is a slight bias in the stellar-mass evolution at constant number density toward higher masses at higher

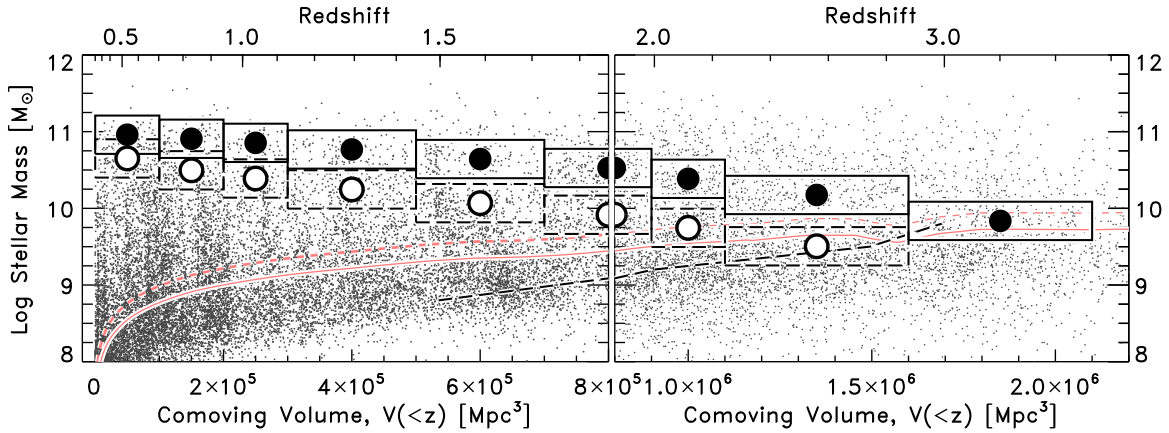

Figure 5. Selection of M^* progenitor galaxies in ZFOURGE. The data points show the stellar masses of all galaxies in the ZFOURGE COSMOS, CDF-S, and UDS fields as a function of comoving volume within each redshift. The scale of the abscissa changes between the left and right panels for clarity. The large circles indicate the central stellar-mass value in bins of comoving volume of the M31-mass (filled circles) and MW-mass (open circles) progenitors selected from the abundance matching of Moster et al. (2013) as described in the text. The solid-line and dashed-line boxes show the bins in comoving volume and stellar mass used to select each progenitor subsample for the M31-mass and MW-mass progenitors, respectively. The volume bin width increases at higher redshift as a trade-off between volume and lookback time. The red curves show the stellar-mass completeness limit for red, passive galaxies defined as a stellar population formed at $z_f = 5$ with no subsequent star formation and no dust extinction for the K_s-band limits derived from simulations for the CDF-S (dashed curve) and UDS (solid curve). The black dashed line shows the 80% completeness limit derived from the comparison to 3D-HST for galaxies at $1.5 < z < 3$.

redshift. For example, the evolution at constant number density from the Tomczak et al. (2013) mass function gives masses larger by $\simeq$0.1–0.2 dex at $z > 2$ for the MW and M31-mass progenitors compared to the abundance-matching results. This is qualitatively consistent with the findings of Leja et al. (2013) and Behroozi et al. (2013a), both of whom find that the number density of galaxy progenitors at higher redshifts shifts to higher values, implying they correspond to lower stellar masses compared to a constant number density selection. The effect is about 0.1 dex from $z = 0$ to 3 (Leja et al. 2013), which is consistent with our observed trend.

Behroozi et al. (2013a) provide the number density evolution of the progenitors of a present-day galaxy population with some ($z = 0$) number density. Figure 4 shows this mass evolution using the median number density evolution from Behroozi et al. with the same literature stellar-mass functions. The evolving number density predicts lower stellar masses compared to the constant number density. The truth is probably inbetween these as the evolving number density predictions assume a dark-matter merger rate that may not track exactly the galaxy merger rate. In many cases, the evolving number density also predicts lower stellar masses compared to either the Moster et al. (2013) and Behroozi et al. (2013b) models. We attribute this to uncertainties in the observed stellar-mass functions at the low-mass end, where small uncertainties in the number densities lead to large uncertainties in the stellar-mass evolution.

Therefore, here we will use the stellar-mass evolution predicted by the abundance matching technique of Moster et al. (2013) to select progenitors of M31- and MW-mass galaxies. The evolution predicted by Moster et al. (2013) is nearly identical to that of Behroozi et al. (2013b; as illustrated in Figure 4), where the latter used a simultaneous fit to the stellar-mass functions, specific SFRs (sSFR), and cosmic SFRs. There is negligible difference in the evolution of the MW progenitors between the two models. The biggest difference is for the M31-mass progenitors (with $z = 0$ stellar mass, $10^{11}\ M_\odot$), where the results of Behroozi et al. (2013b) predict higher stellar masses than those of Moster et al. (2013) with a difference that increases with redshift up to 0.3 dex (factor of $\sim$2) at $z = 3$. Because we select progenitors in bins of $\pm$0.25 dex about the median mass, our results would not change significantly if we used the latter instead. The Moster et al. model predicts a smaller difference in stellar mass between the M31 and MW progenitors at fixed redshift, and therefore our conclusions are, if anything, conservative in that any differences in the populations would presumably be accentuated using the Behroozi et al. model.

Figure 5 shows that the ZFOURGE data set is well matched to track the stellar-mass evolution of MW-like and M31-like galaxies over $0.5 < z < 3$. At lower redshifts, $z < 0.5$, the ZFOURGE data set lacks sufficient volume to track the evolution of galaxies with $M_* \gtrsim 10^{11}\ M_\odot$ down to $z = 0$. However, the ZFOURGE data is sensitive to the progenitors of these galaxies to $z \approx 3.3$, where the expected progenitor mass equals the stellar-mass completeness limit. Similarly, Figure 5 shows that ZFOURGE is complete for progenitors of MW-sized galaxies to $z \approx 2$. Formally, the stellar-mass completeness limit is derived for red, passive stellar populations, whereas the mass limit for blue, star-forming galaxies is lower by about 1 dex. As we show below, nearly all the MW progenitors at these redshifts fall in the latter category, so we expect to track MW progenitors out to $z > 2.5$. Therefore, within the single, homogeneous ZFOURGE data set, we are able to track the evolution of the MW-mass and M31-mass galaxies over a long baseline in time, which corresponds to the majority of the galaxies' formation history.

We select M^* progenitors from ZFOURGE in bins of comoving volume and mass as illustrated in Figure 5. Table 1 lists the redshift intervals, and the central value of the stellar mass used to select the subsamples. We select progenitors of the M31- and MW-mass galaxies that have stellar mass within $\pm$0.25 dex of the central value of stellar mass in each redshift. Our choice of $\pm$0.25 dex in stellar mass is motivated by both the differences in mass evolution based on different abundance matching (or constant number density) methods, and also based on the scatter in the stellar mass of the progenitors of present-day galaxies (see, e.g., Behroozi et al. 2013a). At higher redshift the interval in redshift of the bins increases as a compromise between comoving volume and lookback time spanned by each bin. In the lowest redshift bins there is overlap between the MW and M31 progenitors subsamples (i.e., the boxes overlap in Figure 5). This is

Table 1
Properties of M^* Galaxy Properties

Redshift		Median	Number of Objects per Field			$r_{\rm eff}$		$U-V$	$V-J$	L_{2800}	Quiescent
Range	$\log M_*/M_\odot$	$\log M_*/M_\odot$	CDFS	COSMOS	UDS	(kpc)	n	(mag)	(mag)	($10^9\ L_\odot$)	Fraction
(1)	(2)	(3)	(4)	(5)	(6)	(7)	(8)	(9)	(10)	(11)	(12)
Andromeda-like Progenitors											
$0.2 < z < 0.7$	10.96	10.85	31	18	20	$3.6^{+1.3}_{-1.0}$	$4.2^{+1.3}_{-1.5}$	$2.0^{+0.2}_{-0.2}$	$1.3^{+0.1}_{-0.1}$	$1.7^{+1.4}_{-0.5}$	0.85 ± 0.04
$0.7 < z < 0.9$	10.91	10.81	39	11	19	$3.0^{+1.8}_{-1.1}$	$3.6^{+1.3}_{-1.0}$	$1.9^{+0.2}_{-0.3}$	$1.3^{+0.2}_{-0.2}$	$2.0^{+1.9}_{-0.7}$	0.70 ± 0.05
$0.9 < z < 1.1$	10.85	10.80	15	26	23	$3.2^{+1.4}_{-1.3}$	$3.0^{+1.2}_{-1.3}$	$1.7^{+0.2}_{-0.3}$	$1.4^{+0.2}_{-0.2}$	$4.2^{+4.3}_{-1.1}$	0.47 ± 0.06
$1.1 < z < 1.4$	10.77	10.70	39	23	44	$2.3^{+1.3}_{-1.3}$	$2.5^{+2.5}_{-1.3}$	$1.7^{+0.2}_{-0.4}$	$1.2^{+0.3}_{-0.2}$	$4.4^{+4.5}_{-1.9}$	0.60 ± 0.04
$1.4 < z < 1.7$	10.64	10.62	36	40	63	$1.7^{+1.7}_{-0.9}$	$2.2^{+1.7}_{-1.3}$	$1.6^{+0.3}_{-0.3}$	$1.3^{+0.4}_{-0.2}$	$5.1^{+5.2}_{-2.3}$	0.47 ± 0.04
$1.7 < z < 2.0$	10.53	10.48	59	34	38	$2.1^{+1.9}_{-1.2}$	$1.8^{+1.7}_{-1.1}$	$1.5^{+0.3}_{-0.3}$	$1.3^{+0.4}_{-0.3}$	$4.5^{+5.6}_{-2.2}$	0.33 ± 0.04
$2.0 < z < 2.2$	10.38	10.36	51	29	43	$2.4^{+1.4}_{-1.4}$	$1.0^{+1.5}_{-0.5}$	$1.2^{+0.5}_{-0.4}$	$1.1^{+0.5}_{-0.4}$	$7.3^{+5.7}_{-4.5}$	0.31 ± 0.03
$2.2 < z < 2.8$	10.17	10.15	57	67	86	$2.1^{+1.1}_{-0.9}$	$1.1^{+2.0}_{-0.6}$	$0.9^{+0.6}_{-0.3}$	$0.8^{+0.5}_{-0.4}$	$13.5^{+11.9}_{-7.8}$	0.13 ± 0.02
$2.8 < z < 3.5$	9.84	9.80	95	72	77	$1.2^{+0.9}_{-0.4}$	$1.3^{+1.9}_{-0.7}$	$0.6^{+0.4}_{-0.3}$	$0.3^{+0.9}_{-0.6}$	$20.6^{+9.9}_{-8.3}$	0.04 ± 0.01
MW-like progenitors											
$0.2 < z < 0.7$	10.65	10.60	59	45	47	$2.6^{+1.5}_{-1.1}$	$3.4^{+1.7}_{-1.7}$	$1.9^{+0.2}_{-0.3}$	$1.3^{+0.2}_{-0.1}$	$1.3^{+1.4}_{-0.4}$	0.74 ± 0.03
$0.7 < z < 0.9$	10.50	10.47	81	36	43	$2.1^{+1.4}_{-1.0}$	$2.7^{+1.4}_{-1.4}$	$1.7^{+0.2}_{-0.3}$	$1.3^{+0.3}_{-0.2}$	$1.5^{+1.6}_{-0.6}$	0.54 ± 0.03
$0.9 < z < 1.1$	10.39	10.35	44	43	35	$2.3^{+2.2}_{-1.3}$	$2.1^{+1.5}_{-1.2}$	$1.6^{+0.3}_{-0.3}$	$1.2^{+0.4}_{-0.2}$	$2.3^{+3.1}_{-0.9}$	0.41 ± 0.04
$1.1 < z < 1.4$	10.25	10.21	78	69	81	$2.2^{+1.6}_{-1.1}$	$1.5^{+2.1}_{-0.8}$	$1.4^{+0.4}_{-0.4}$	$1.2^{+0.4}_{-0.3}$	$3.4^{+5.4}_{-1.9}$	0.29 ± 0.03
$1.4 < z < 1.7$	10.07	10.06	82	67	99	$2.1^{+1.3}_{-1.0}$	$1.2^{+1.5}_{-0.6}$	$1.1^{+0.5}_{-0.3}$	$1.0^{+0.4}_{-0.3}$	$5.5^{+6.1}_{-3.6}$	0.20 ± 0.02
$1.7 < z < 2.0$	9.92	9.88	84	51	75	$2.2^{+1.2}_{-0.9}$	$1.1^{+1.1}_{-0.6}$	$0.9^{+0.4}_{-0.3}$	$0.8^{+0.5}_{-0.4}$	$8.9^{+9.2}_{-5.3}$	0.12 ± 0.02
$2.0 < z < 2.2$	9.75	9.70	102	70	93	$1.7^{+0.8}_{-0.6}$	$1.3^{+1.4}_{-0.6}$	$0.6^{+0.4}_{-0.3}$	$0.5^{+0.4}_{-0.3}$	$11.7^{+5.5}_{-5.0}$	0.06 ± 0.01
$2.2 < z < 2.8$	9.51	9.48	173	197	224	$1.3^{+0.8}_{-0.5}$	$1.3^{+1.4}_{-0.7}$	$0.6^{+0.3}_{-0.3}$	$0.3^{+0.5}_{-0.4}$	$13.0^{+6.4}_{-4.8}$	0.03 ± 0.01

Notes. (1) Redshift range of bin. (2) Central value of the stellar mass used to select progenitors in the redshift bin; galaxies are selected within ±0.25 dex of this value in this bin. (3) Median stellar mass of selected galaxies in the redshift bin. (4)–(6) Number of objects selected in this redshift range and stellar-mass bin from the CDFS, COSMOS, and UDS ZFOURGE data. (7) Effective radius of progenitors measured from CANDELS WFC3 F160W imaging. (8) Sérsic index measured from CANDELS WFC3 F160W imaging. (9) and (10) Rest-frame $U-V$ and $V-J$ color indices measured from ZFOURGE multiwavelength data. (11) Rest-frame luminosity at 2800 Å derived from the ZFOURGE data. Errors on (4)–(11) are the 68% percentile range of the distribution. (12) Fraction of quiescent galaxies, defined as the ratio of the number of galaxies with quiescent $U-V$ and $V-J$ colors to the total number in each bin. Errors on (12) are derived using a bootstrap Monte Carlo simulation.

acceptable because the scatter in the progenitor mass evolution means that the descendants of the galaxies in the overlap region may become either MW- or M31-mass galaxies at $z \sim 0$ (again, see discussion in, e.g., Behroozi et al. 2013a). Table 1 lists the number of galaxies from each ZFOURGE field, and the median mass of the galaxies selected in each subsample. Table 1 also lists the median and 68 percentile range on the distribution of the $U-V$ and $V-J$ rest-frame color, and the effective radius and Sérsic index of the galaxies in each subsample of M^* galaxies.

5. COLOR EVOLUTION OF M^* GALAXIES

Figure 6 shows the evolution of the rest-frame $U-V$ and $V-J$ colors (a *UVJ* diagram) of the M31- and MW-mass galaxy progenitors from $z = 0.5$ to 3. The rest-frame *UVJ* color–color plane separates galaxies that are actively star-forming from those in quiescent phases of evolution (e.g., Labbé et al. 2005; Wuyts et al. 2007; Williams et al. 2009; Whitaker et al. 2011; Papovich et al. 2012; Morishita et al. 2014). Galaxies that fall in the star-forming region of the *UVJ* diagram have high current SFRs compared to their past average. In contrast, galaxies in the quiescent region of the *UVJ* diagram have current SFRs much lower than their past average. The sequence of star-forming galaxies follows dust attenuation as the colors move along the *UVJ* diagram from relatively unattenuated galaxies with blue $U-V$ and $V-J$ colors to those with higher dust attenuation and red $U-V$ and $V-J$ colors.

Figure 7 shows that both the M31- and MW-mass progenitors have similar evolution in their median $U-V$ and $V-J$ color with redshift. However, the changes in the galaxies occur at earlier times (higher redshifts) for the higher-mass M31 progenitors compared to the lower-mass MW progenitors. At the highest redshifts ($z \gtrsim 2.5$), the progenitors are blue in both their $U-V$ and $V-J$ colors, indicating they are star forming with relatively low dust attenuation. As the population moves to lower redshifts ($1.6 \lesssim z \lesssim 2.5$), the $U-V$ and $V-J$ colors become redder, indicating they are star forming but with higher dust attenuation, and there are essentially *no* blue, unattenuated galaxies. At redshifts less than about $z \lesssim 1$, the progenitors become a mix of galaxies with dust-attenuated star-forming galaxies and quiescent objects whose star formation is quenching. The color evolution reflects this as an increasing portion of the evolution occurs as a reddening of the median $U-V$ color. As a result, by $z \lesssim 0.5$ the majority of both the MW and M31 progenitors have crossed into the quiescent region, indicating these galaxies have either quenched their star formation, or are forming stars at rates much less than their past average.

While the M31-mass and MW-mass progenitors follow similar color-evolutionary paths, they do so at different stellar masses. Figure 8 shows the evolution between the median rest-frame colors as a function of mass and redshift. At fixed *stellar mass* the massive M31-mass progenitors have bluer rest-frame $U-V$ and $V-J$ colors compared to the less massive MW-mass

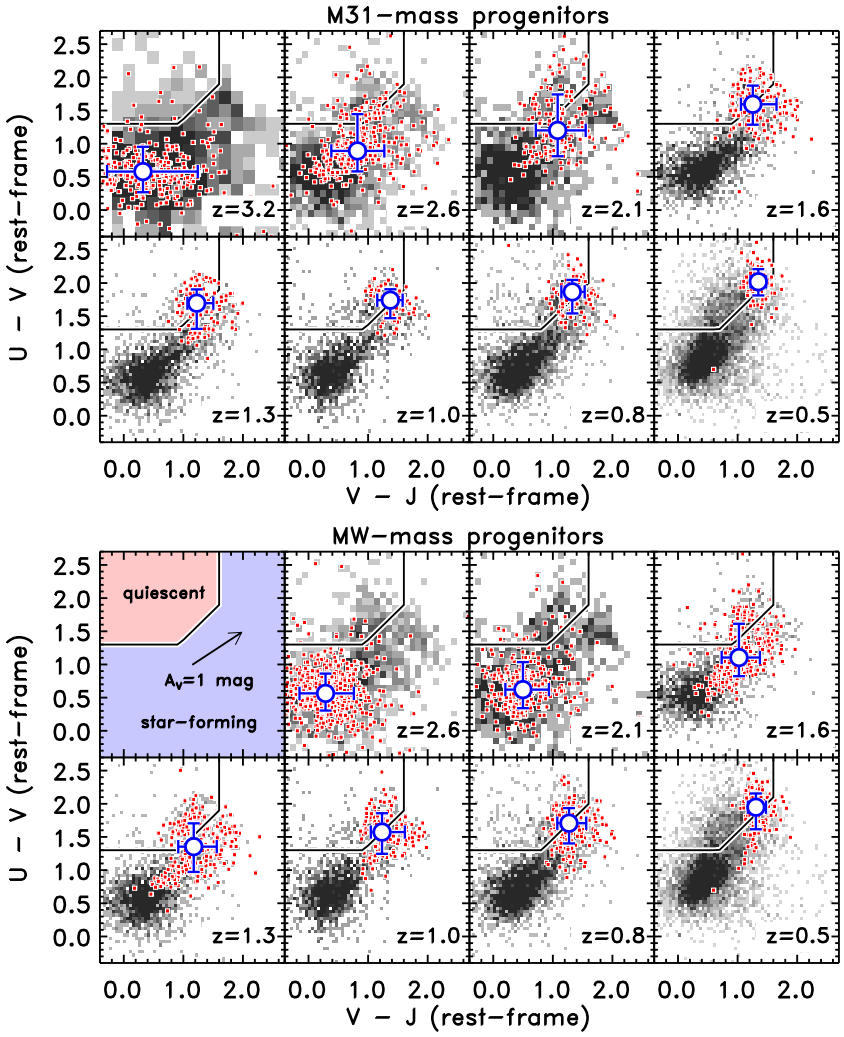

Figure 6. Evolution of rest-frame $U-V$ and $V-J$ color distributions of progenitors of M31-mass and MW-mass galaxies. The polygon in each panel delineates "quiescent" galaxies (upper left region) from "star-forming" (everywhere else) using the definition of Williams et al. (2009), as indicated in the top left panel of the MW-mass progenitor plot. The arrow in that panel shows the effects on the colors for $A_V = 1$ mag of dust attenuation for the starburst dust model (Calzetti et al. 2000). In both plots the grayscale increases with the density of all galaxies in the ZFOURGE catalogs that have those rest-frame colors in each redshift bin. The red points in each panel show the M^* galaxy progenitors. The top figure shows the color evolution of M31-mass progenitors, and the bottom figure shows MW-mass progenitors. The large circles in each bin show the median value of the M^* galaxy progenitors in each panel. The error bars show the 68th percentile range of rest-frame colors for the M31-mass and MW-mass progenitors.

progenitors. Therefore the color evolution is dependent both on stellar mass and redshift.

The M31 progenitors become quiescent at earlier times (higher redshift) compared to the lower-mass MW progenitors. Figure 9 shows the evolution in the quiescent fraction of the M31 and MW progenitors, where the quiescent fraction is defined as the ratio of the total number of galaxies falling in the "quiescent" region of the UVJ diagram to the total number of galaxies in each progenitor sample at each redshift. We derived uncertainties on the quiescent fraction using a bootstrap Monte Carlo simulation. We reconstructed each subsample repeatedly with the same number of galaxies in each reconstruction, but randomly drawing from each subsample with replacement. We took as the uncertainty the standard deviation using the normalized median absolute deviation of the distribution of quiescent fractions from the reconstructions (see Brammer et al. 2008). The quiescent fractions are listed in Table 1. At all redshifts, the quiescent fraction of the M31 progenitors is higher. For both the M31 and MW progenitors, as they become quiescent, their stellar populations homogenize. This is evident from the low scatter on the quiescent fraction and the UVJ colors (where the error bars span the inter-68th percentile), where the low scatter implies similar mass-dominated stellar population ages within each subsample.

6. MORPHOLOGICAL EVOLUTION OF THE M^* GALAXIES

Figure 10 shows that the size evolution of the M31-mass and MW-mass progenitor samples. At $z > 2$ the M31-mass progenitors are small (1–2 kpc) albeit with significant scatter about the median. Although there is significant scatter about the median, the error on the medians are much smaller (as there are more than 60 galaxies in each bin of redshift). This yields a measurement of the rate of size growth in these galaxies that is generally consistent with the growth of disks within galaxy halos, where $r_{\rm eff} \propto H(z)^{-1}$ (under the assumption of a constant halo spin parameter, Mo et al. 1998; Ferguson et al. 2004) Quantitatively, a fit of the function $r_{\rm eff} \propto H(z)^{-1}$ to the data for the M31-mass progenitors extrapolates to $r_{\rm eff}(0) =$

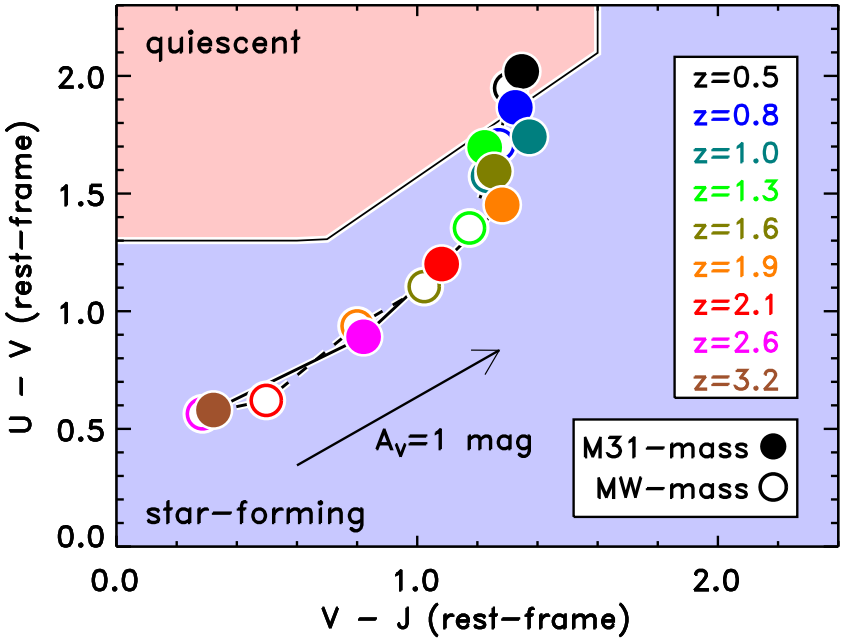

Figure 7. Evolution in the median $U-V$ and $V-J$ color for the MW-mass progenitors (open symbols connected by dashed lines) and M31-mass progenitors (filled symbols connected by solid lines). Each point shows the median color at each redshift as indicated by color (see figure inset). As in Figure 6, the polygon denotes the region in the upper left populated by quiescent galaxies. The arrow shows the effects on the colors for $A_V = 1$ mag of dust attenuation for the starburst dust model (Calzetti et al. 2000). The MW- and M31-mass progenitors follow similar color evolution, but the more massive M31-mass progenitors evolve earlier (at higher redshift) compared to the less massive MW progenitors.

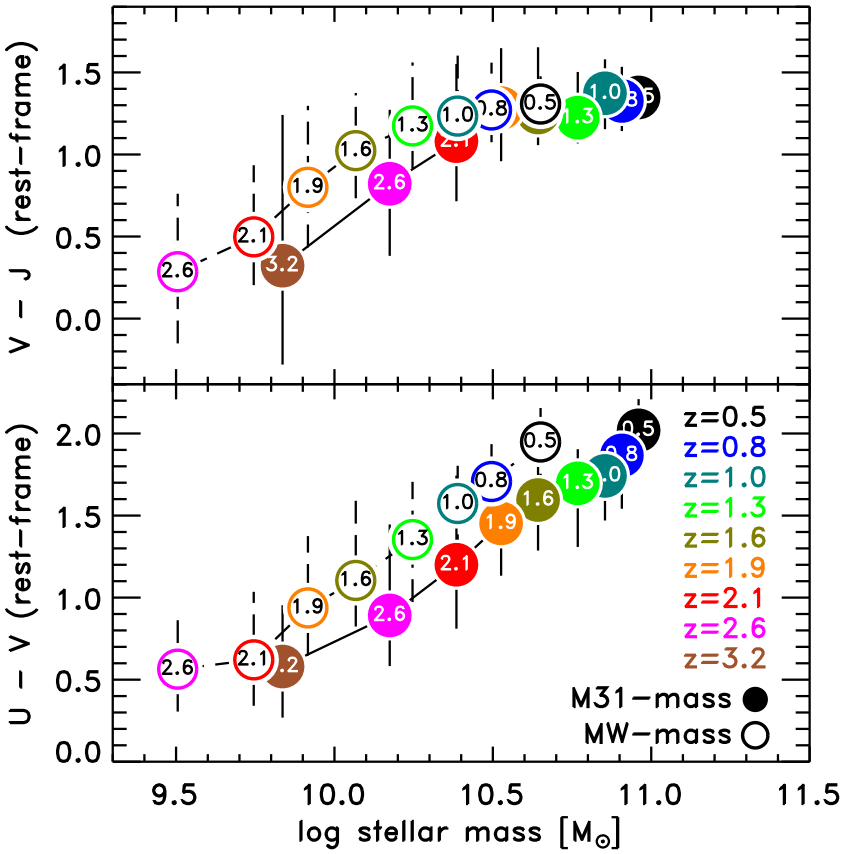

Figure 8. Evolution in the median $U-V$ and $V-J$ color as a function of stellar mass for the MW-mass progenitors (open symbols connected by dashed lines) and M31-mass progenitors (filled symbols connected by solid lines). Each point shows the median color at each redshift as indicated by its label and color (see figure inset). The error bars span the inter-68th percentile of each subsample. While the MW- and M31-mass progenitors follow similar color evolution, the M31-mass progenitors achieve redder colors at higher fixed stellar mass compared to the lower mass MW-mass progenitors.

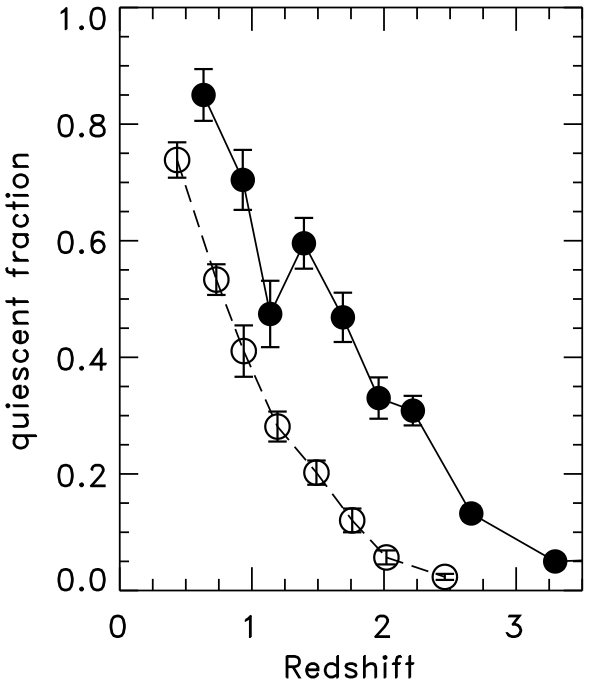

Figure 9. Evolution of the fraction of quiescent galaxies for M^* galaxies as a function of redshift. The filled circles and solid line show the evolution of the M31-mass progenitors. The open circles and dashed line show the evolution of the MW-mass progenitors. The quiescent fraction of the MW and M31 progenitors increases with decreasing redshift, although at all redshifts the M31 progenitors have a higher quiescent fraction.

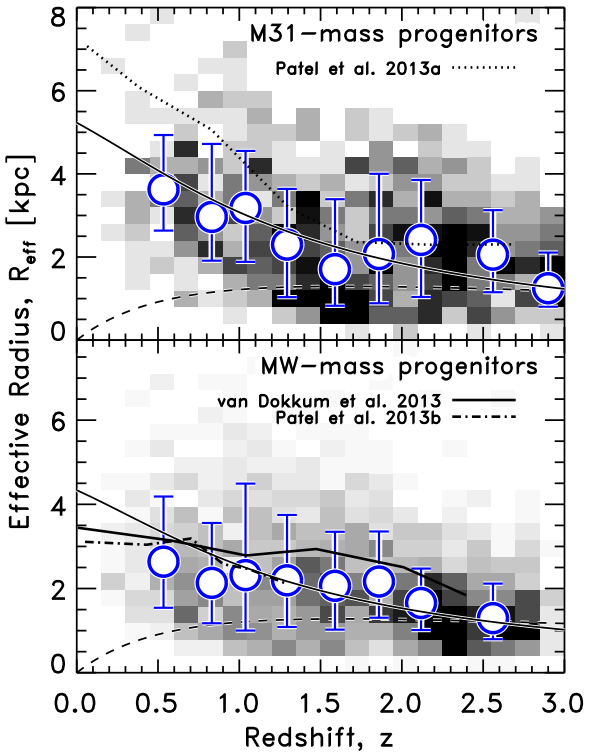

Figure 10. Size evolution of M31-mass (top panel) and MW-mass (bottom panel) galaxies. In each panel, the shaded regions show the density of data points that fall in that bin. The large blue circles are the median in bins of redshift, and the error bars show the 68th percentile range of the distribution. The dashed line shows the FWHM *HST*/WFC3 PSF. The solid line shows a fit to the medians where the effective size scales with the inverse Hubble parameter, $R_{\rm eff} \propto H(z)^{-1}$. The curves show relations for other galaxy samples taken from the literature.

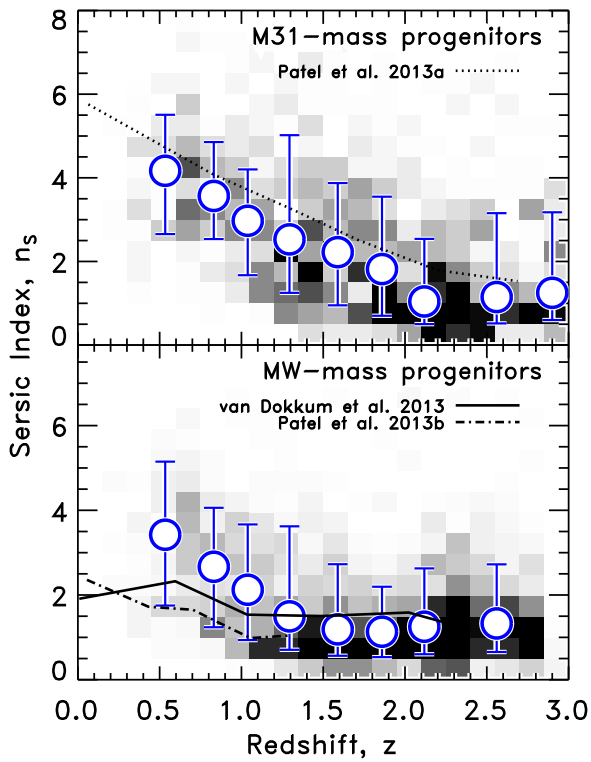

Figure 11. Sérsic index evolution of M31-mass (top panel) and MW-mass (bottom panel) galaxies. In each panel, the shaded regions show the density of data points that fall in that bin. The large blue circles are the median in bins of redshift, and the error bars show the 68th percentile range on the distribution. The curves show relations for other galaxy samples taken from the literature.

5.2 ± 0.1 kpc at $z = 0$. A fit to a more generic function, $r_{\rm eff} \propto (1+z)^{\gamma}$ returns $\gamma = -1.0 \pm 0.05$. Similarly, the MW-mass progenitors are uniformly small at $z \gtrsim 2$, with $r_{\rm eff} \sim$ 1–2 kpc. A fit to the data assuming $r_{\rm eff} \propto H(z)^{-1}$ extrapolates to $r_{\rm eff}(0) = 4.3 \pm 0.05$ kpc at $z = 0$. A fit to the function $r_{\rm eff} \propto (1+z)^{\gamma}$ returns $\gamma = -0.9 \pm 0.05$. There is clear evidence for size growth in both the M31-mass and MW-mass progenitors, consistent with the growth of disks. This is consistent with other studies (see Patel et al. 2013a, 2013b; van Dokkum et al. 2013, and discussion below).

The median Sérsic index of the M^* galaxy progenitors evolves smoothly with redshift, as shown in Figure 11. At the highest redshifts, both the M31 and MW progenitors have low Sérsic indices, with median $\langle n_s \rangle \simeq 1$ for $z > 2$ for the M31-mass progenitors, and $z > 1.5$ for the MW-mass progenitors, consistent with exponentially declining disk-like surface-brightness profiles. As the galaxies evolve to lower redshift, both the M31- and MW-mass progenitors begin a monotonic increase in their median Sérsic indices with decreasing redshift, from a median value of $\langle n_s \rangle \simeq 1$ at $z = 2$ to $\langle n_s \rangle = 4$ at $z = 0.5$ for the M31-mass progenitors, and $\langle n_s \rangle \simeq 1$ at $z = 1.3$ to $\langle n_s \rangle = 3.5$ at $z = 0.5$ for the MW-mass progenitors. Equating larger values of n_s with bulge formation, it is during these periods when M^* galaxies grow their spheroids.

As with the size evolution, the evolution in the Sérsic index is not driven by the morphological K corrections arising from using a fixed observed band (WFC3 F160W). The Sérsic indices derived from the WFC3 F105W change only slightly from the values from the WFC3 F160W imaging, and this change does not affect the qualitative conclusions.

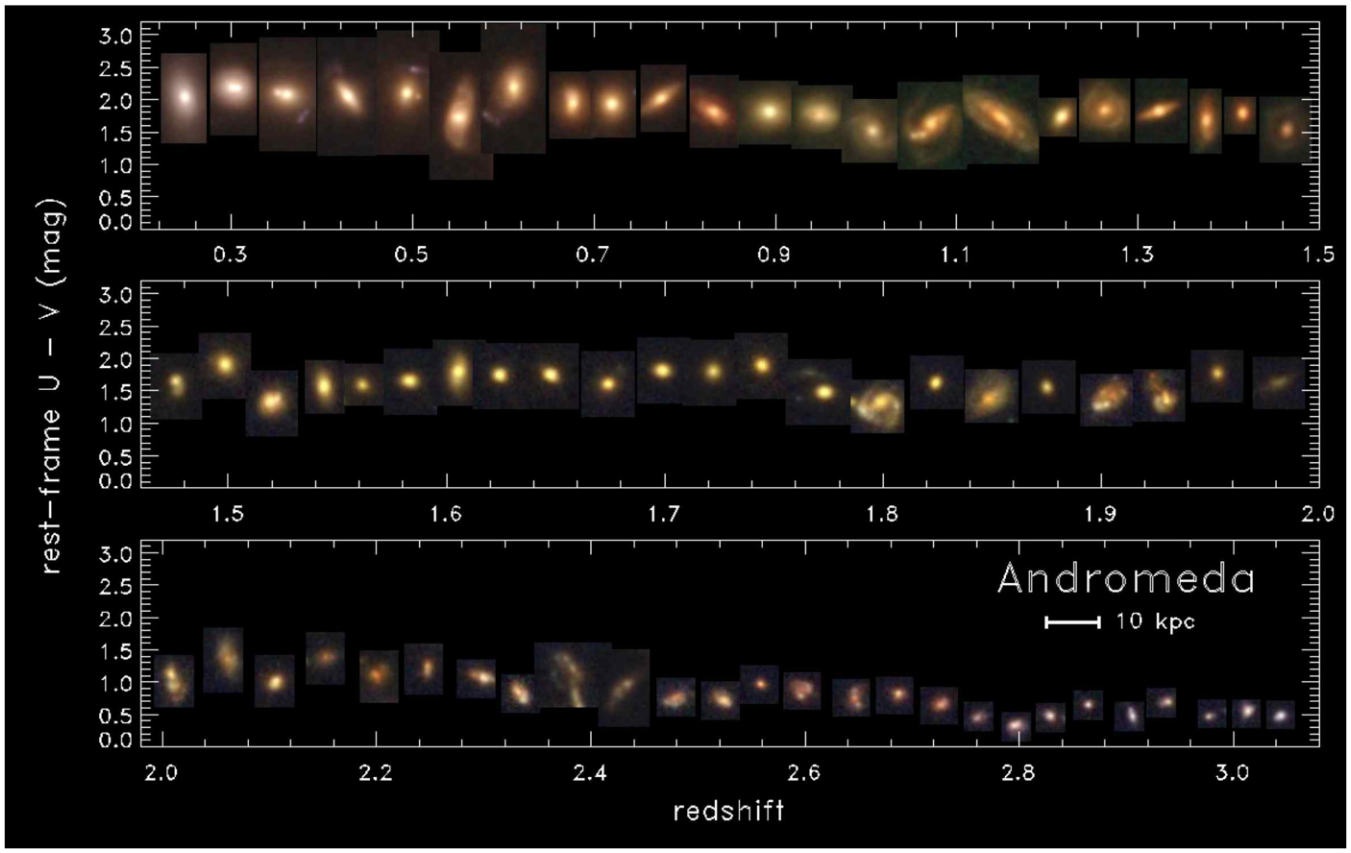

Figure 12. Examples of progenitors of an M31-mass galaxy from $z = 3$ to the $z = 0.5$. Each galaxy is selected such that it has the (approximate) median $U - V$ and $V - J$ color derived for all progenitors in a given redshift bin (see Table 1). Each false-color image shows the approximate rest-frame U, B, V band (blue, green, red, respectively) using the ACS ($B_{435}V_{606}i_{775}z_{850}$) and WFC3 ($J_{125}H_{160}$) band closest to rest-frame UBV at each redshift (for this reason we show only progenitors from the CDF-S sample because this full complement of *HST* imaging does not exist for the COSMOS nor the UDS ZFOURGE fields; see Grogin et al. 2011; Koekemoer et al. 2011). The images are placed at their measured rest-frame $U - V$ color and redshift (slight adjustments in redshift are made for presentation purposes, but the rank order of the galaxies is unchanged). The image sizes are scaled to the same fixed physical scale where the inset shows a scale of 10 kpc.

Our results compare favorably with those in the literature. Patel et al. (2013b) considered the size evolution of galaxies selected to have constant number density, $\log(n/\mathrm{Mpc}^{-3}) = -3.9$, slightly less common (and therefore more massive) than the M31-mass progenitors in our sample (the latter have number density closer to $\log[n/\mathrm{Mpc}^{-3}] = -3.4$; see Figure 4). Figures 10 and 11 show that the galaxies in the Patel et al. sample have larger effective radii and larger Sérsic indexes compared to our values for the M31-mass progenitors at the same redshift. This is likely a result of the higher stellar masses of the galaxies studied by Patel et al. compared to the M31-mass sample here. The differences could be related to band-shifting effects ("morphological K corrections"), as Patel et al. use ACS F814W imaging for their sample at $z < 1$ where we use WFC3 F160W (see also van der Wel et al. 2014). There is only a slight increase in $r_{\rm eff}$ of our sample derived with the WFC3 F105W compared to the F160W band (the median increases by ≈10% at $z = 0.5$; see also Morishita et al. 2014). Therefore, the choice of bandpass for the effective sizes does not change the qualitative conclusions.

van Dokkum et al. (2013) considered the evolution of the Sérsic index of MW-sized progenitors and derive a somewhat different evolution. As illustrated in Figures 10 and 11, by $z \sim 2$, the galaxies in their sample have already achieved higher Sérsic index, $n_s \sim 2$, higher than those in our sample, with somewhat higher effective radii at higher redshifts. It is likely this is because the van Dokkum et al. sample is selected to have constant number density, which yields higher stellar-mass progenitors at $z \sim 2$ ($\log M_*/M_\odot \gtrsim 10$). In comparison, the progenitors in our MW-mass sample are lower in stellar mass by about a factor of two at $z \sim 2$. Because the evolution is such that at fixed redshift the median Sérsic index increases with stellar mass, the difference in stellar mass between the samples likely accounts for the difference in Sérsic-index evolution.

Patel et al. (2013a) traced the structural evolution of star-forming MW-mass progenitors from $z \sim 0$ to $z = 1.5$. Their sample was selected using the inferred growth from the star-forming sequence (see Leitner 2012). The galaxies in their progenitor sample have lower stellar mass (by about 0.2 dex) compared to our MW-progenitor sample. Figures 10 and 11 show while the evolution in effective radius is similar between their sample and ours, the galaxies in their sample have weaker evolution in Sérsic index, with $\langle n_s \rangle \simeq 1.5$–2 at $z \sim 0.4$ compared to our finding of $\langle n_s \rangle = 3.4$ at $z = 0.5$. This difference is likely due entirely to the fact that the Patel et al. samples are star forming only, with lower stellar mass.

The visual morphology of the progenitors of M31-mass and MW-mass galaxies encapsulates their evolution, as illustrated in Figures 12 and 13. Each figure shows (approximate) rest-frame UBV images of galaxies from the progenitor subsamples that have the median $U - V$ and $V - J$ colors derived in Figure 6 for the M31- and the MW-mass subsamples, respectively. Specifically, we select from the progenitors those galaxies satisfying $(\Delta_{UV}^2 + \Delta_{VJ}^2)^{1/2} \leqslant 0.3$ mag, where $\Delta_{UV} \equiv \langle (U - V) \rangle - (U - V)$

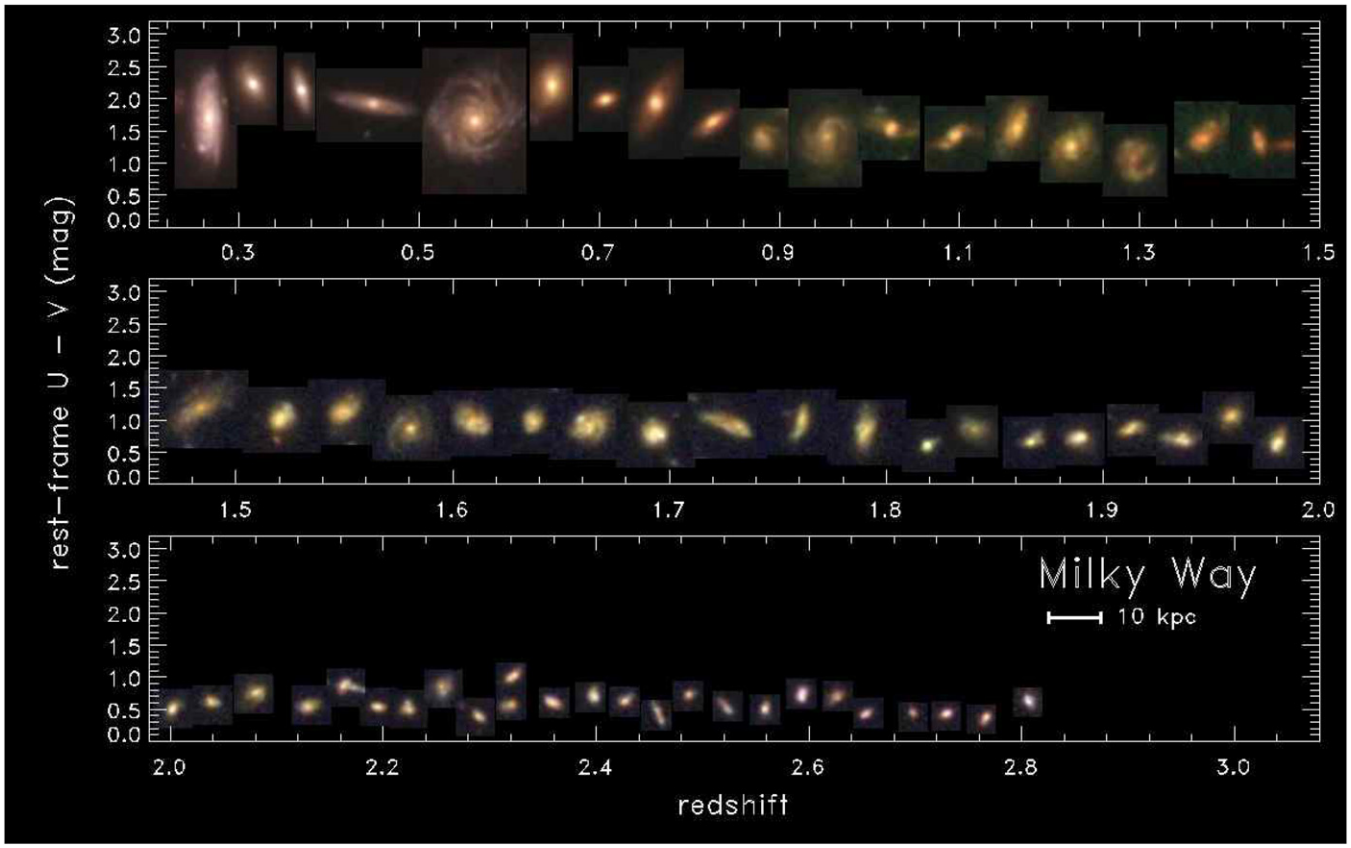

Figure 13. Same as Figure 12, but for progenitors of MW-mass galaxies from $z = 3$ to the $z = 0.5$.

and $\Delta_{VJ} \equiv \langle (V-J) \rangle - (V-J)$ is the color difference between the median color and the color of each galaxy the MW- and M31-mass progenitors in each redshift bin. We selected galaxies at random from the subsample that satisfies this color selection. We visually inspected cases where galaxies overlapped on the figure, rejecting objects to ensure that the figure captures the diversity of morphology. At the highest redshifts, the M31- and MW-mass progenitors are small and blue, with visual morphologies similar to UV-selected Lyman-break galaxies (LBGs; e.g., Papovich et al. 2005). Starting around $z \sim 2$ the progenitors become more diffuse and nebulous, sometimes with redder cores and blue outskirts, and some showing star-forming (blue) clumps (similar in morphology to those in other star-forming galaxies at these epochs; e.g., Elmegreen et al. 2008). Starting around $z \sim 1$–1.5 more mature morphological structures form, and some of the progenitors develop spiral arms, and spheroid/disk combinations: it appears that $z \sim 1$ is the epoch where M^* galaxies begin to populate the "Hubble sequence."[38] At $z \lesssim 1$ the morphologies of the M^* progenitors have matured, and all the progenitors show either early-type morphologies and/or bulge-dominated disks, including examples of "grand design spirals."

Comparing Figures 12 and 13, with those of "modern-day" M^* galaxies from SDSS at $0.02 < z < 0.03$ in Figures 2 and 3 above, we see they dovetail nicely. The morphologies of the $z \sim 0.5$ M^* galaxies show examples of spheroid galaxies, bulge-dominated disk galaxies, and grand design spirals.

[38] Some of the M31-mass progenitors at $z \sim 1.5$–1.7 show compact (spheroidal) morphologies. These may be outliers as these images are all taken from the GOODS-S, which is known to host an overdense large-scale structure at $z \sim 1.6$ (Kurk et al. 2009; Giavalisco et al. 2011). There is evidence that galaxies in overdense regions have accelerated morphological evolution, (e.g., Papovich et al. 2012; Bassett et al. 2013; Delaye et al. 2014), which may account for the more early-type morphologies of the M31 progenitors at this redshift in this field.

7. EVOLUTION OF THE IR EMISSION AND THE SFR

7.1. Stacked IR Images and the Total IR Emission

The majority of the galaxies in both the M31 and MW progenitor samples are undetected in the *Spitzer*/MIPS 24 μm and *Herschel*/PACS 100 and 160 μm imaging. The fraction of sources detected at 24 μm ($>5\sigma$) is less than 50% for $z < 1$, and this declines to <30% at $z = 1.9$ and <10% at $z > 2$. At all redshifts, the objects *detected* in the MIPS and PACS data represent only the most luminous galaxies at each redshift, forming a biased subset. Therefore, to study the evolution in the far-IR emission from the galaxies in the M31- and MW-progenitor samples we stack the mid- and far-IR data to improve the effective depth. By doing this we lose the ability to study galaxies on an object-by-object basis, but we gain the ability to measure the average 24, 100, and 160 μm emission for these samples to fainter flux densities than otherwise possible. Stacking techniques have proven valuable to study the IR emission from faint galaxy populations (e.g., Dole et al. 2006; Zheng et al. 2006, 2007; Dye et al. 2007; Huynh et al. 2007; Papovich et al. 2007; Lee et al. 2010; Rodighiero et al. 2010; Schreiber et al. 2014). Papovich et al. (2007) showed that for sources with flux densities about a factor of two lower than the formal signal-to-noise ratio (S/N) = 5 detection limit, one can recover the average stacked fluxes accurate to better than 10% for sufficiently large samples ($N > 100$–200 objects).

Table 2
Stacked IR Properties, SFRs, and Implied Gas Fractions of M^*-galaxy Progenitors

z (1)	N (2)	$F_\nu(3.6\,\mu\mathrm{m})$ (μJy) (3)	$F_\nu(4.5\,\mu\mathrm{m})$ (μJy) (4)	$F_\nu(24\,\mu\mathrm{m})$ (μJy) (5)	$F_\nu(100\,\mu\mathrm{m})$ (μJy) (6)	$F_\nu(160\,\mu\mathrm{m})$ (μJy) (7)	$L_{\rm IR}$ ($10^{11}\,L_\odot$) (8)	SFR ($M_\odot \mathrm{yr}^{-1}$) (9)	$f_{\rm gas}$ (10)
M31-mass Progenitors									
0.5	100	115.6 ± 5.1	81.4 ± 4.5	50.6 ± 10.7	1217 ± 247	2410 ± 612	0.22 ± 0.03	2.8 ± 0.8	0.03 ± 0.01
0.8	115	70.6 ± 3.6	48.1 ± 2.4	73.9 ± 16.3	1240 ± 276	2973 ± 828	0.77 ± 0.11	8.4 ± 1.7	0.06 ± 0.02
1.0	78	57.5 ± 2.4	46.4 ± 2.5	129.9 ± 19.3	2188 ± 403	5918 ± 1118	2.22 ± 0.22	23.6 ± 3.6	0.13 ± 0.03
1.3	136	32.0 ± 1.6	29.7 ± 1.3	60.1 ± 7.4	1124 ± 283	2524 ± 706	2.53 ± 0.26	26.7 ± 4.1	0.14 ± 0.04
1.6	175	16.7 ± 0.76	18.4 ± 0.71	55.0 ± 7.8	844 ± 127	2171 ± 403	3.30 ± 0.30	34.6 ± 4.7	0.19 ± 0.04
1.8	209	9.6 ± 0.35	11.3 ± 0.37	76.7 ± 8.0	894 ± 111	2409 ± 366	4.74 ± 0.34	48.9 ± 4.9	0.30 ± 0.06
2.1	175	5.5 ± 0.22	6.4 ± 0.30	60.0 ± 3.6	528 ± 96.3	1284 ± 302	3.89 ± 0.22	41.3 ± 4.6	0.36 ± 0.08
2.6	350	3.2 ± 0.11	3.7 ± 0.13	28.5 ± 2.6	409 ± 60.8	763 ± 245	4.78 ± 0.37	52.2 ± 8.1	0.50 ± 0.13
3.2	406	1.1 ± 0.06	1.3 ± 0.06	2.8 ± 1.0	76.0 ± 43.9	45.3 ± 189	1.48 ± 0.48	21.8 ± 11.8	0.47 ± 0.30
MW-mass Progenitors									
0.5	191	74.9 ± 2.5	51.8 ± 2.2	61.7 ± 14.1	1374 ± 201	3129 ± 597	0.28 ± 0.03	3.3 ± 0.7	0.05 ± 0.02
0.8	221	38.1 ± 1.3	26.5 ± 0.90	89.6 ± 12.6	1562 ± 196	3463 ± 467	0.96 ± 0.07	10.1 ± 1.2	0.13 ± 0.03
1.0	165	27.0 ± 0.88	21.4 ± 0.95	103.5 ± 9.4	1841 ± 169	4937 ± 528	1.81 ± 0.10	18.8 ± 1.8	0.23 ± 0.04
1.3	290	13.1 ± 0.51	12.5 ± 0.46	47.1 ± 1.9	922 ± 82.5	2367 ± 302	2.03 ± 0.07	21.4 ± 1.8	0.32 ± 0.06
1.6	356	6.5 ± 0.19	7.4 ± 0.21	45.3 ± 2.7	668 ± 76.3	1404 ± 278	2.69 ± 0.14	28.7 ± 3.2	0.46 ± 0.09
1.8	291	4.2 ± 0.18	4.6 ± 0.22	38.5 ± 3.2	485 ± 58.3	1395 ± 305	2.53 ± 0.17	28.3 ± 4.6	0.55 ± 0.15
2.1	370	2.2 ± 0.12	2.3 ± 0.12	16.4 ± 1.8	238 ± 58.6	526 ± 189	1.50 ± 0.15	18.9 ± 5.3	0.54 ± 0.22
2.6	869	1.1 ± 0.04	1.1 ± 0.04	5.2 ± 1.0	67.7 ± 36.4	202 ± 141	0.85 ± 0.15	12.8 ± 5.8	0.57 ± 0.32

Notes. (1) Redshift of bin, (2) number of objects stacked in each bin, (3–7) measured flux density from the IRAC 3.6 μm, 4.5 μm, MIPS 24 μm, PACS 100 μm, and 160 μm, respectively, (8) total IR luminosity derived from the stacked MIPS and PAC photometry, (9) total SFR derived from the $L_{\rm IR}$ and rest-frame luminosity at 2800 Å, (10) implied gas-mass fraction, defined as $M_{\rm gas}/(M_* + M_{\rm gas})$.

Here, we used the method described in Papovich et al. (2007) to stack the IR emission for all the galaxies in each redshift bin for the M31- and MW-mass progenitor samples. We stacked the galaxies in the MIPS 24 μm, and PACS 100 and 160 μm data using the M^* progenitor samples in each redshift bin discussed in Section 4. We stacked the IRAC data in addition to the MIPS/PACS data to provide a reference between the stacked far-IR data and the near-IR data (see below). We first take a small subimage of $100'' \times 100''$ from the 3.6, 4.5, 24, 100, and 160 μm data for each source to be stacked. We used a two-dimensional bilinear interpolation to center the subimage on the astrometric coordinates of each source. We then subtracted a local background from each source using the sky value measured in a bandpass-dependent annulus using values from the literature (Popesso et al. 2012; Magnelli et al. 2013)[39,40,41] centered on each source. Following Papovich et al. (2007) we rotated each subimage randomly by 0°, 90°, 180°, or 270° to suppress any image artifacts, which tend to be aligned in either detector rows or columns. We stack the images, taking the mean of all pixels (after clipping $>3\sigma$ outliers) that contribute to a given pixel in the final stack. We measured the flux densities in circular apertures of radius 2.″4, 2.″4, 3.″5, 7″, and 12″, correcting for light outside those apertures by multiplying the fluxes by factors of 1.20, 1.22, 2.57, 1.47, and 1.45 for IRAC 3.6, 4.5 μm, MIPS 24 μm, and *Herschel* 100, 160 μm, respectively, using values from documentation[39,40,41] and the literature (Popesso et al. 2012; Magnelli et al. 2013). Table 2 lists the measured flux densities from the stacks.

We estimated uncertainties for the stacked flux densities using a bootstrap Monte Carlo simulation. For each subsample, we repeated the stacking procedure 100 times. Each time we constructed a new subsample equal in size to the original subsample, but which contained randomly selected galaxies from the original subsample with replacement. We then recomputed the flux density from the stack of the random subsample. The estimate of the uncertainty is the standard deviation of the distribution of the measured flux densities from these Monte Carlo simulations (in this way the estimated uncertainties are the uncertainty on the median). Table 2 lists these uncertainties.

We also stacked on random positions in the images as a secondary estimate of the uncertainties on the flux densities. For our stacking we did not remove flux from detected IR sources because some of the M^* progenitors are directly detected, and we did not want introduce biases by erroneously subtracting the light from sources in our sample that may be undetected but otherwise blended with nearby sources. Rather we tested how this affects our measurements by using the random stack to measure any bias resulting from stacking procedure. We stacked a number of random pointings equal to the number of sources in each subsample (where we have made no requirement on the location of the random pointings, which can fall on or near detected IR sources), and we repeated this step >500 times. We then computed the mean and standard deviation of the flux density distribution from the random stacks. For large numbers of sources, $N > 10^5$, the mean flux density from the stack at random positions is small, $\langle f_\nu \rangle = (-0.015, -0.015, 0.6, -24,$ and 47 μJy) at (3.6, 4.5, 24, 100, and 160 μm), respectively. In all cases, this bias is much lower than the uncertainty, with S/N < 0.3 for the size subsamples here. Similarly, for all samples except those at the highest redshift, the standard deviation from the random stacks is much smaller than the uncertainties computed above. Therefore, variations of the IR emission within the progenitor samples dominate the uncertainties of the stacked flux densities. In the cases of the highest redshift

[39] http://irsa.ipac.caltech.edu/data/SPITZER/docs/irac
[40] http://irsa.ipac.caltech.edu/data/SPITZER/docs/mips
[41] http://herschel.esac.esa.int/twiki/pub/Public/PacsCalibrationWeb/pacs_bolo_fluxcal_report_v1.pdf

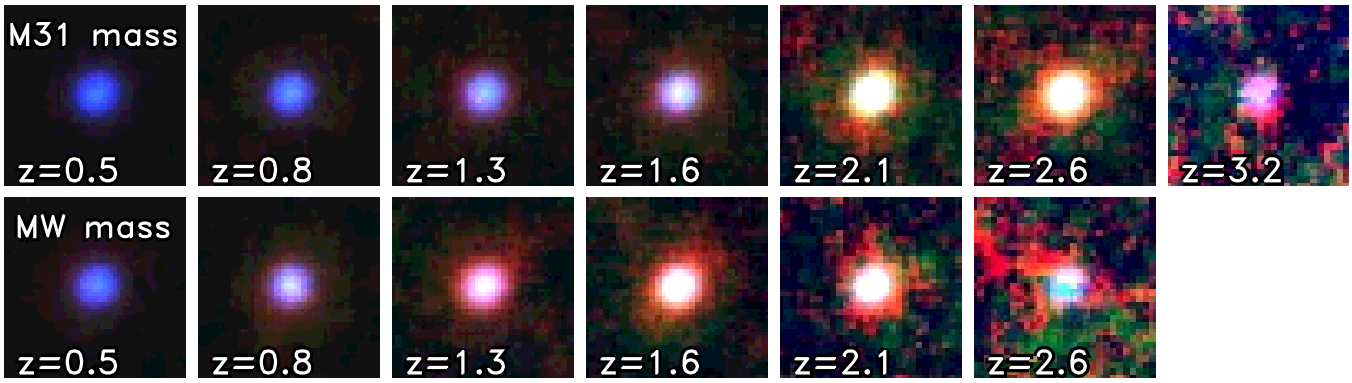

Figure 14. Stacked false-color infrared images for the progenitors in the M31-mass and MW-mass galaxy subsamples. The top row shows the redshift evolution of M31-mass progenitors and the bottom row shows the redshift evolution of MW-mass progenitors. In each panel, the false-colors show the stacked IRAC 3.6 + 4.5 μm flux density (blue), the stacked MIPS 24 μm flux density (green), and the mean of the PACS 100 and 160 μm flux density (red). The scaling in the false-color images is tilted so that a source will appear white if it has a spectral energy distribution that follows $f_\nu \sim \lambda^{1.5}$. The images have not been matched in their point-response functions (PRFs). The PRFs between MIPS 24 μm and *Herschel* 100 μm are about equal (both have PRF FWHM $\simeq 6''$), but are larger than that of IRAC (PRF FWHM $\simeq 1''.6$).

subsamples ($z = 3.1$ for the M31-mass progenitors and $z = 2.5$ for the MW-mass progenitors), the uncertainty from the random stacks (at 24, 100, and 160 μm) are approximately equal to those from our Monte Carlo simulation above. This implies that the image noise (a combination of sky and confusion noise) dominates the uncertainties in the stack for these subsamples. Because our results from the Monte Carlo simulation on the galaxy subsamples include both the variation in the IR emission of the subsample and effects from the sky noise, we adopt these uncertainties here.

Figure 14 shows images of the stacked IRAC, MIPS, and PACS data for each of the redshift subsamples for the M31- and MW-progenitor samples. While *K*-corrections in the bandpasses persist, in general, the blue color of the progenitors at $z \sim 0.5$ means that direct starlight traced in the IRAC bands exceeds the reprocessed dust emission traced by the far-IR data. The white color of the progenitors at higher redshifts, $2.1 \leqslant z \leqslant 2.6$ for M31, and $1.6 \leqslant z \leqslant 2.1$ for the MW, means that the dust-reprocessed emission contributes more to the bolometric emission than the direct starlight.

For each subsample of the M31- and MW-mass progenitors, we fitted template IR spectral energy distributions (Rieke et al. 2009) to the stacked 24, 100, and 160 μm flux densities and their uncertainties from the stacks to estimate total IR luminosities, $L_{\rm IR} = L(8\text{–}1000\,\mu{\rm m})$, and their uncertainties (where these are the uncertainties on the median). These are listed in Table 2. Because the IR flux densities cover the mid-IR (the Wein side of the thermal emission) to the far-IR wavelengths (covering the peak of the thermal dust emission), the choice of IR spectral templates makes only a small difference in the total IR luminosities. Using the Chary & Elbaz (2001) or Dale et al. (2005) templates changes the derived IR luminosities by $<30\%$ (0.1 dex). Our choice to use the Rieke et al. templates is motivated by the fact that these templates better reproduce the far-IR flux ratios of observed galaxies at high redshifts (see the discussion in Rieke et al. and Shipley et al. 2013).

Figure 15 shows the evolution of the IR spectral energy distributions for the M31- and MW-mass progenitors. At $z = 0.5$ the emission from direct starlight is larger than the dust-reprocessed emission for the M31-mass progenitors by a large factor, and for the MW progenitors the stellar light and dust-reprocessed emission are comparable. As the redshift increases, the far-IR emission increases relative to the near-IR emission, such that the far-IR emission dominates the bolometric output for $1 \lesssim z \lesssim 2.6$. At the highest redshifts, $z = 3.2$ for M31 and $z = 2.6$ for the MW, the contribution from the thermal far-IR emission to the bolometric emission declines. Because these galaxies are all star-forming with very blue rest-frame *UVJ* colors, there is less dust (and lower obscuration) in these galaxies.

Figure 16 shows the evolution of the inferred $L_{\rm IR}$ from $z = 0.5$ to 3. The IR luminosity of both the M31- and MW-mass progenitors rise from the highest redshifts, $z = 2.5$ (3.2 for the M31-mass progenitors) to reach a plateau for $1 < z \lesssim 2$ (2.5 for the case of M31-mass progenitors). Both progenitor populations show a marked decrease in $L_{\rm IR}$ from $z = 1$ to 0.5. The M31-mass progenitors have a higher peak $L_{\rm IR}$ (by more than a factor of two) compared to that of the MW progenitors. The M31 progenitors reach their peak earlier in their evolution, at $z \simeq 1.8$–2.5, and sustain this peak for a longer duration, compared to the MW progenitors, which reach their peak IR luminosity at $z \simeq 1.6$.

Although active galactic nuclei (AGNs) are likely rare in the M^* progenitor samples, they do occur in hosts with stellar masses $\gtrsim 10^{10}\,M_\odot$ (e.g., Kauffmann et al. 2004; Cardamone et al. 2010), and could contribute to the stacked IR emission. We matched all objects in the progenitor samples to the CANDELS-matched X-ray catalogs for the CDF-S and COSMOS fields (Kocevski et al. 2012; D. D. Kocevski et al., in preparation). Likely AGN, with $L_X > 10^{43}$ erg s^{-1}, account for $<8\%$ of the progenitors in any subsample at any redshift. We excluded these sources and restacked the IR luminosity for each subsample, which lowered the implied IR luminosities by <0.1 dex for all samples at all redshifts. Because star formation likely contributes to the IR emission even in galaxies hosting AGNs (e.g., Shipley et al. 2013), on average AGNs do not strongly contribute to the IR luminosity for the MW-mass and M31-mass progenitors.

7.2. Evolution of the IR/UV Ratio

The total IR luminosities allow us to study the evolution of the IR/UV luminosity ratio, defined here as the ratio of the total IR luminosity to the rest-frame luminosity at 2800 Å (where L_{2800} has no correction for dust attenuation), $L_{\rm IR}/L_{2800} \equiv L_{\rm IR}/L_{\rm UV}$. The top panel of Figure 16 shows the evolution of this ratio for the M31- and MW-mass progenitors.

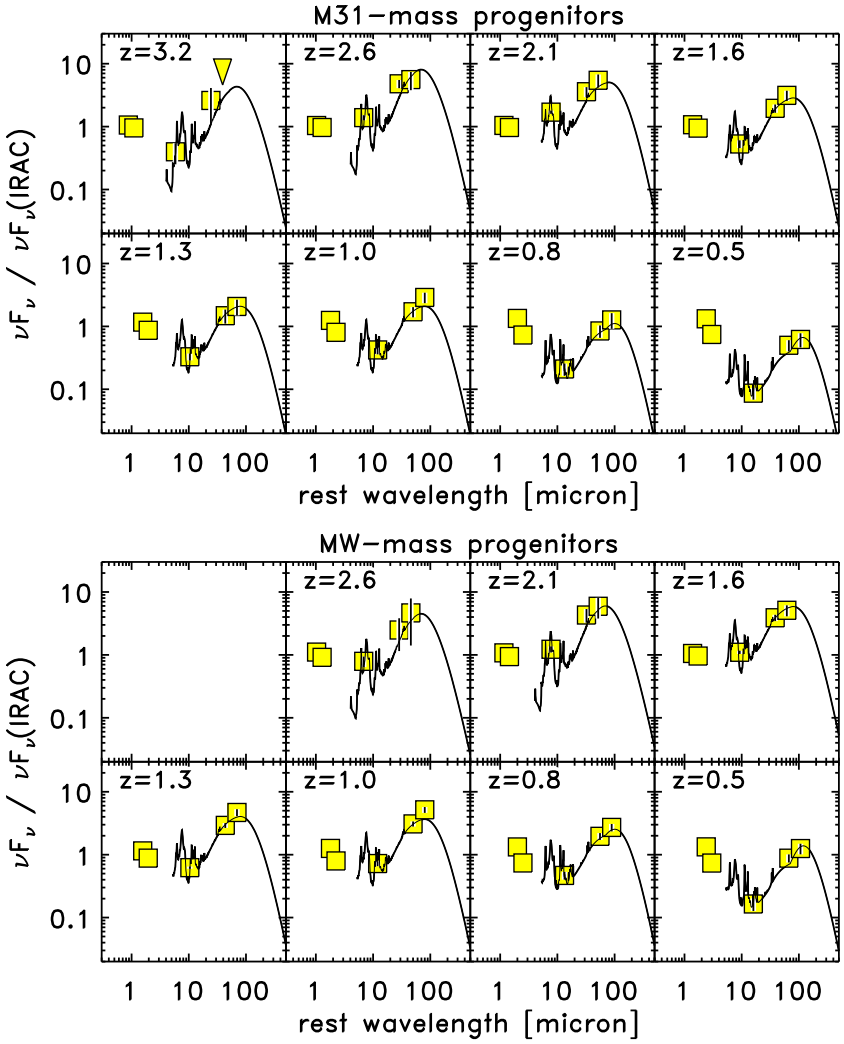

Figure 15. Evolution of the IR spectral energy distributions of M^* galaxy progenitors. The top figure shows the evolution of M31-mass progenitors, and the bottom figure shows the evolution of the MW-mass progenitors. In each panel of each figure, the yellow filled boxes show the stacked flux densities from IRAC 3.6, 4.5 μm, MIPS 24 μm, and PACS 100, 160 μm for each subsample in redshift, normalized to the average IRAC 3.6 and 4.5 μm data. The uncertainties are derived using the Monte Carlo simulation described in the text. Downward triangles show 2σ upper limits for IR flux densities with measured $f_\nu/\sigma(f_\nu) < 1$. The line in each panel shows the best-fit Rieke et al. (2009) IR template spectral energy distribution. We infer the total $L_{\rm IR} = L(8\text{–}1000\,\mu{\rm m})$ IR luminosity by integrating the best-fit template for each subsample.

The evolution in $L_{\rm IR}/L_{\rm UV}$ is similar for both the M31- and the MW-mass progenitors. At the highest redshifts, $z = 3.2$ for the M31-mass, and $z = 2.5$ for the MW-mass progenitors $L_{\rm IR}/L_{\rm UV} < 10$, which is typical for LBGs (Reddy et al. 2010). The $L_{\rm IR}/L_{\rm UV}$ values increase with time (decreasing redshift), peaking at $L_{\rm IR}/L_{\rm UV} \approx 100$ at $z \sim 2$ and $z \sim 1$ for the M31-mass and the MW-mass progenitors, respectively. These ratios are more typical of ultra luminous IR galaxies (Papovich et al. 2006; Reddy et al. 2010). The implication is that these progenitor galaxies are producing and retaining greater amounts of dust, which then absorb radiation from star formation, re-emitting in it the far-IR.

At lower redshifts, $L_{\rm IR}/L_{\rm UV}$ drops to $\approx$10 at $z = 0.5$. The fact $L_{\rm IR}/L_{\rm UV}$ declines implies the IR luminosity is declining faster than the rest-frame UV. The SFR is declining, and/or that there is a reduction in the density of dust in the galaxy (perhaps as a result of the declining gas density, see Section 7.4, and a constant gas-mass-to-dust-mass ratio for fixed metallicity; e.g., Bell 2003).

7.3. Evolution of the SFR and Specific SFR

Nearly all the bolometric emission from star formation is emitted in the UV and IR (see discussion in, e.g., Bell 2003). We use the SFR conversion from the combination of the UV and IR luminosities (Bell et al. 2005; Papovich et al. 2006) to estimate the instantaneous SFRs for the M31- and MW-mass progenitors,

$$\Psi/M_\odot\ {\rm yr}^{-1} = 10^{-10}(L_{\rm IR} + 3.3L_{2800})/L_\odot, \qquad (2)$$

based on the calibration presented by Kennicutt (1998a), and the constant of proportionality is adjusted for the Chabrier IMF assumed here. Table 2 gives the derived SFRs.

Figure 17 shows the SFR history for the MW- and M31-mass galaxies. The SFRs of the MW- and M31-mass progenitors are already high ($>10\,M_\odot$ yr^{-1}) at the highest redshifts to which we can observe them. The SFRs peak around $z = 2$–2.5 for the M31-mass progenitors (with a peak value of $\Psi \simeq 50\,M_\odot$ yr^{-1}) and around $z = 1.5$ for the MW progenitors (with a peak value

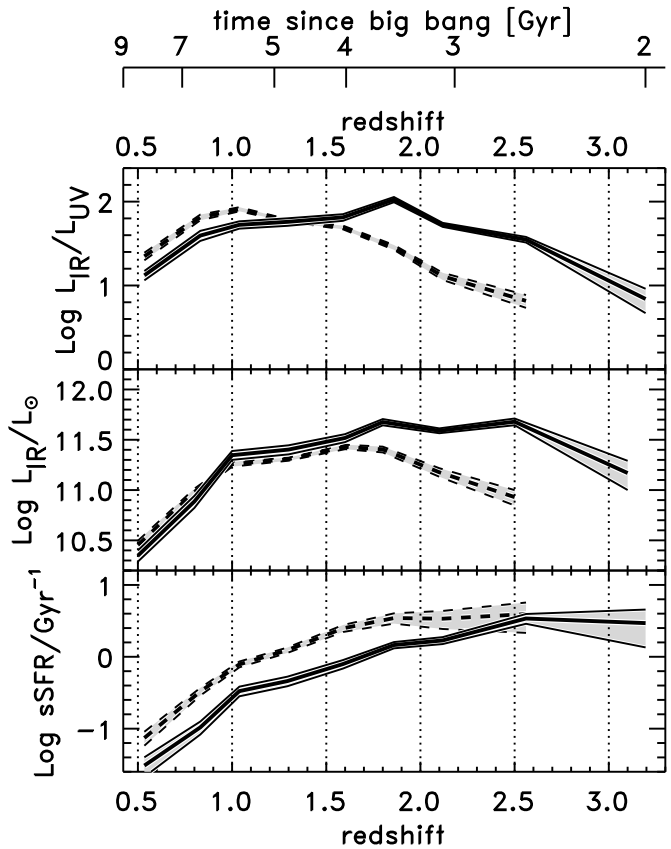

Figure 16. Evolution of the IR/UV ratio (top panel) total IR luminosity (middle panel), and specific SFR (sSFR; bottom panel). In all panels, the solid lines show the evolution of the M31-mass progenitors, the dashed lines show the evolution of the MW-mass progenitors, and the estimated uncertainties on the median value.

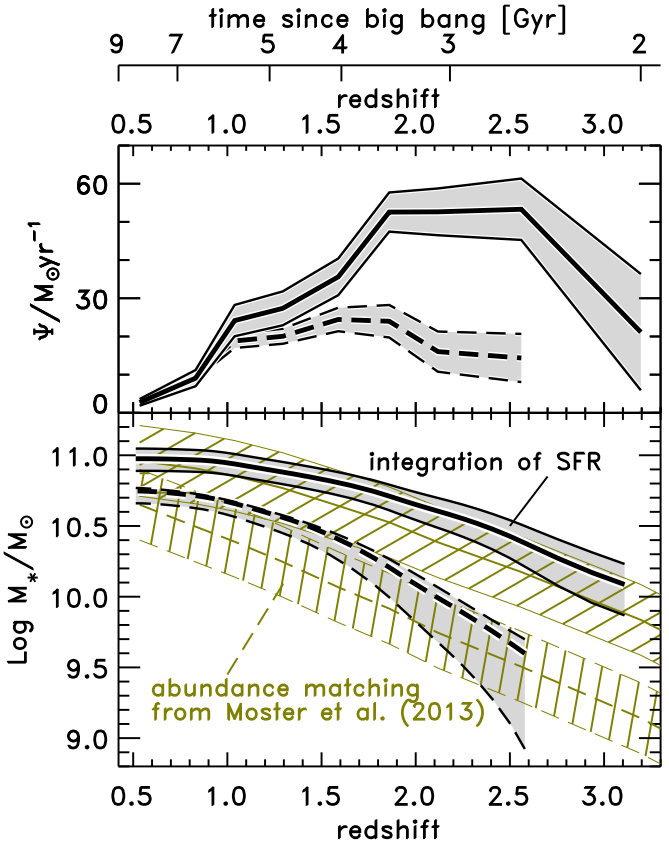

Figure 17. Evolution of the SFR, Ψ, and the stellar mass derived from the integrated SFR history. The top panel shows the SFR evolution for the M31-mass (solid lines) and MW-mass (dashed lines) progenitors, where the width of each region corresponds to the inter-68th percentile. The bottom panel shows the integrated SFR history, derived by using the SFR evolution with the Bruzual & Charlot (2003) stellar population synthesis models. The shaded regions correspond to the M31-mass (solid lines) and MW-mass (solid lines) progenitors, respectively, as in the top panel. The hashed regions in the bottom panel show the stellar-mass evolution from the abundance matching (Moster et al. 2013) used to the select the progenitor galaxy samples. While there is some offset, there is general agreement between the models and the data.

$\Psi \simeq 30\,M_{\odot}$ yr^{-1}). The SFRs are nearly equal for both the M31 and MW progenitors at $z \sim 1$, and they decline at about the same rate to values of a few solar masses per year at $z = 0.5$ (and this decline continues to the present; the current SFR of the MW and M31 galaxies proper is 0.5–1.5 $M_{\odot}$ yr^{-1}, see Mutch et al. 2011). The observed SFR evolution in Figure 17 matches qualitatively with that derived from complex abundance matching (Behroozi et al. 2013c) and from modeling galaxy spectra (Pacifici et al. 2013). Because these results are independent and based on very different analyses and data sets, the level of agreement and the fact that we are settling on a mean SFR history for galaxies with the stellar masses of M31 and the MW is encouraging (see also, Patel et al. 2013a; van Dokkum et al. 2013).

Figure 16 shows the evolution of the sSFR. The behavior of the sSFR is approximately the same for both the M31- and MW-mass progenitors, but they are offset in redshift. The M31-mass progenitors have a plateau in log (sSFR/Gyr^{-1}) $\approx$ 0.5 for $z \geqslant 2.5$, with a steady decline toward lower redshift. The magnitude of this plateau in sSFR is consistent with other studies of star-forming galaxies at $z > 2$ (see Reddy et al. 2012, and references therein). The MW-mass progenitors have a similar plateau with the same value for $z \geqslant 1.8$, and also show a steady decline toward lower redshift. This follows from the fact that at $z \lesssim 1$ the SFR evolution is nearly identical for both the MW- and M31-mass progenitors, but because the MW-mass progenitors have lower stellar mass, they have higher sSFRs.

Figure 17 shows that the SFR history inferred from the IR and UV data for the M31- and MW-mass progenitors agrees with the stellar-mass evolution derived by Moster et al. (2013), which was used to select the progenitors themselves. We obtain the stellar-mass evolutions by integrating the SFR histories with the Bruzual & Charlot (2003) stellar population synthesis model. At intermediate redshifts, the integrated SFR histories rise faster than that predicted by the Moster et al. abundance matching. This may be because our measurements of the SFR histories have a coarse sampling in cosmic time (averaged over bins of redshift spanning at least ≈10% of a Hubble time at each redshift), whereas the abundance matching is more continuous with redshift: our integrated SFR histories may lack the time resolution needed to recover the exact stellar-mass evolutions. Regardless, the offset is not large (within the 0.25 dex spread on the stellar mass history), and the consistency between the stellar mass from the abundance matching and the integrated SFR history is reassuring that the SFR history is a reasonable representation of that of M^* galaxies such as M31 and the MW.

7.4. Evolution of the Implied Gas Fraction

The surface density of SFR is correlated with the local surface density of cold gas in galaxies through the established Kennicutt–Schmidt law (Schmidt 1959; Kennicutt 1998b). Therefore, the measured SFRs and sizes of the M^* galaxies

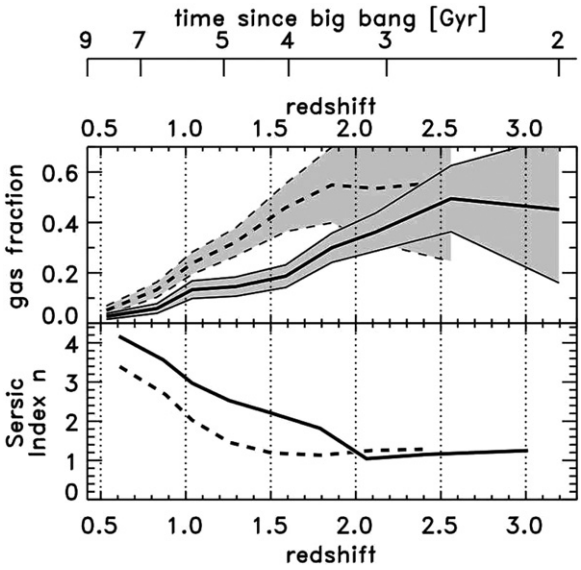

Figure 18. Evolution of the implied gas fraction of M^* galaxies. The top panel shows the evolution of the gas fraction, defined as $f_{\rm gas} = M_{\rm gas}/(M_{\rm gas} + M_*)$. The solid lines show the median and 68 percentile range for the M31-mass progenitors and the dashed lines show the median and 68 percentile range for the MW-mass progenitors. The bottom panel reproduces the average evolution of the Sérsic evolution for the M31- and MW-mass progenitors as solid and dashed lines, respectively. The evolution of the gas fraction is anticorrelated with the Sérsic index.

constrain the gas-mass surface density (and therefore the implied gas mass). Inverting the relation between the local gas-surface density and the SFR surface density gives

$$\frac{M_{\rm gas}}{6.8\times10^8\ M_\odot} = \left(\frac{\Psi}{1\ M_\odot\ {\rm yr}^{-1}}\right)^{5/7}\left(\frac{r_{\rm eff}}{1\ {\rm kpc}}\right)^{4/7}, \quad (3)$$

as in Papovich et al. (2011, see also Conselice et al. 2013). Using this equation, we derived gas masses for our progenitor samples using the effective sizes ($r_{\rm eff}$) and SFRs (Ψ) from Tables 1 and 2. The gas fraction is given by comparing the gas masses with the stellar masses by

$$f_{\rm gas} = \frac{M_{\rm gas}}{M_{\rm gas} + M_*}. \quad (4)$$

Table 2 gives the gas-mass fractions for each of the progenitor subsamples.

Figure 18 shows the evolution of these (implied) gas fractions for the M31- and MW-mass progenitor samples. The gas fractions are $f_{\rm gas} \simeq 0.4$–0.6 at $z > 2.5$ for the M31-mass progenitors (and at $z > 2$ for the MW-mass progenitors). Such high gas fractions are consistent with values derived for other star-forming galaxies at these redshifts, $z > 2$, which have $f_{\rm gas} \sim 0.3$–0.5 for galaxies with stellar masses $\log M_*/M_\odot = 9.5$–10.4 (e.g., Erb et al. 2006; Daddi et al. 2010; Förster-Schreiber et al. 2009; Tacconi et al. 2010, 2013).

Figure 18 also shows that the average gas-mass fractions for the M^*-galaxy progenitors decline monotonically with decreasing redshifts. There are strong trends in stellar mass. For the more massive M31-mass galaxies, this decrease in the gas-mass fraction begins by $z \simeq 2.5$, whereas it occurs later (by $z \sim 2$) for the less massive MW-mass galaxies. The direction of this trend is also consistent with Conselice et al. (2013), who find gas fractions 0–0.2 for most galaxies with $\log M_*/M_\odot > 11$ at $z > 1.5$. The decline in the implied gas-mass fractions of the M^* galaxies continues with decreasing redshift. By $z \sim 0.5$ the values for the M^* progenitor samples are very low: the median values are $f_{\rm gas} = 0.03$ for M31 and 0.05 for the MW. Furthermore, Figure 18 shows that the decline in the average gas-mass fraction is simultaneous with an increase in the Sérsic index for the M^* progenitor samples.

Our implied gas-mass fractions for the M^* progenitors are $\langle f_{\rm gas}\rangle = 0.03$–$0.05$ by $z \sim 0.5$. Saintonge et al. (2011) find that nearby galaxies ($D_L < 200$ Mpc) with detected H_2 molecular gas and stellar masses $\log M_*/M_\odot = 10.7$–11 have implied total cold gas fractions $f_{\rm gas} \simeq 0.07$–0.11 (albeit with appreciable galaxy-to-galaxy scatter). Similar results are found by Morganti et al. (2006), but see also the discussion in Young et al. (2009). The observed cold gas fractions from Saintonge et al. are *higher* by about a factor of two compared to the gas fractions we infer for the M^* progenitors here. One reason to expect this difference is that the M^*-galaxy progenitors may contain additional cold gas, but that the star formation efficiency is necessarily low such that this gas does not contribute to the SFR (as we derive the implied gas fractions inverting the Kennicutt–Schmidt law). We discuss this further below.

8. DISCUSSION

8.1. The Growth of M^* Galaxies

8.1.1. The LBG Phase

To the highest redshifts at which we are able to observe them, the MW- and M31-mass galaxy progenitors exist as UV-luminous, star-forming galaxies with relatively low obscuration at $z \sim 2$–2.5 and $z = 3.2$, respectively. Their stellar masses, (blue) rest-frame colors, and small effective sizes are typical of the well-studied ($R \lesssim 25$ mag) LBG and Lyα emitter (LAE) populations at these redshifts (e.g., Steidel et al. 1999; Giavalisco 2002; Papovich et al. 2001, 2005; Gawiser et al. 2007; Shapley et al. 2001; Shapley 2011; Nilsson et al. 2011; Vargas et al. 2014). Although at our highest-redshift bins, our samples could be biased against progenitors that are redden by dust or quiescent stellar populations, we argue this is not the case for the reasons in Section 3.2. During these star-forming stages more than 50% of the present-day stellar-mass is formed in M^*-mass progenitors. This conclusion is consistent with that of van Dokkum et al. (see also Patel et al. 2013b, 2013). These redshifts mark the "LBG phase" of MW-mass and M31-mass progenitors, and it seems likely that the main progenitors of both the MW and M31 would have existed as LBGs 10–11 Gyr ago.

During this phase the typical main progenitors of M^* galaxies are star-forming disks ($n_s \simeq 1$; Figure 11). At these redshifts, the implied gas fractions in these disks are high because the SFRs are high and the scale radii small (Section 7.3 and Figure 18). These disks are likely gas rich and highly turbulent, similar to dispersion-dominated star-forming disks measured in higher mass galaxies at these redshifts (e.g., Genzel et al. 2008; Förster Schreiber et al. 2011). Because the Sérsic indices show no evidence for evolution at these redshifts, the progenitors are predominantly disks. Therefore, it is either the case that any physical processes capable of transferring (e.g., clump migration, disk instabilities) or redistributing mass (e.g., mergers) to a bulge/spheroid are not acting in a substantial way for M^* progenitor galaxies, or that any process that transfers material to the center must be counterbalanced by continued mass growth (i.e., via accretion) in the outskirts in such a way that the Sérsic index stays low while the total stellar mass and radius both grow.

8.1.2. The Luminous IR-galaxy Phase

All indications based on the rest-frame color evolution (Figures 6 and 7), the IR-luminosity evolution, and L_{IR}/L_{UV} evolution (Figure 16) show that the dust obscuration increases as the M^* progenitors form their stars. The measured L_{IR}, SFRs, and L_{IR}/L_{UV} ratios all peak during this period ($1 < z < 2$) and then they decline at lower redshift ($z \lesssim 1$). At the end of these phases, the M^* galaxies have formed >75% of their present-day stellar mass. Most of the stars in galaxies such as M31 and the MW formed their stars during the first ~6 Gyr of the history of the universe.

Figure 17 also shows that essentially *all* of the stellar-mass growth in M31-mass and MW-mass progenitors can be accounted for by the measured SFR evolution from the UV and IR observations. Therefore, there is little room for *ex situ* mass (i.e., mass in stars accreted directly in small satellites) to contribute to the stellar-mass evolution for present-day M^* galaxies at least for $z \lesssim 2$–3. Similar results are also derived independently by van Dokkum et al. (2013) and Patel et al. (2013a), and are similar to the findings by Moster et al. (2013) and Behroozi et al. (2013c) based on independent abundance matching methods for dark-matter halos hosting present-day M^* galaxies.

8.1.3. Quiescent Transition Phase

During the luminous IR galaxy phase, some of the progenitors of MW-mass and M31-mass galaxies remain in stages of dust-obscured star formation, but the quiescent fraction steadily grows with decreasing redshift (Figure 9). The increase in the fraction of quiescent galaxies is simultaneous with an increase with the morphological Sérsic index, where the quiescent fraction reaches ≈50% when the Sérsic index reaches $n_s \simeq 2$. As the quiescent fraction and Sérsic index increase, the implied gas fraction decreases. The anticorrelation between the Sérsic index and star formation activity is consistent with other findings between star formation and increasing stellar-mass surface density and bulge growth (e.g., Kauffmann et al. 2003; Franx et al. 2008; Bell et al. 2012; Papovich et al. 2012; Bassett et al. 2013; Patel et al. 2013b). Figure 19 shows the evolution of the Sérsic-index against the implied gas fraction for the M^* progenitors. The evolution is nearly indistinguishable for the MW- and M31-mass progenitors. Therefore, the redshift-dependent differences in the evolution of M^* galaxies divides out when considering the Sérsic index–gas fraction plane. This is evidence that the formation of bulges coincides with the decline in the gas fraction.

Lastly, it seems unlikely that major mergers dominate the assembly of M^* galaxies as they move through the quiescent transition phase. If major mergers are frequent, then we could expect larger scatter in colors of the M31- and MW-mass progenitor galaxies (see Figure 8), unless the timescales for these are so short that the median color evolution remains smooth. Several studies found that major mergers seem insufficient to produce the observed abundance of spheroidal galaxies (including, for example, Jogee et al. 2008; Bundy et al. 2009; Stewart et al. 2009). Additional evidence disfavoring major mergers comes from the facts that the mass growth from star formation accounts for the stellar-mass growth from abundance matching (Figure 17; Moster et al. 2013; Behroozi et al. 2013c), and approximately accounts for all the mass evolution from constant number density (see Figure 4).

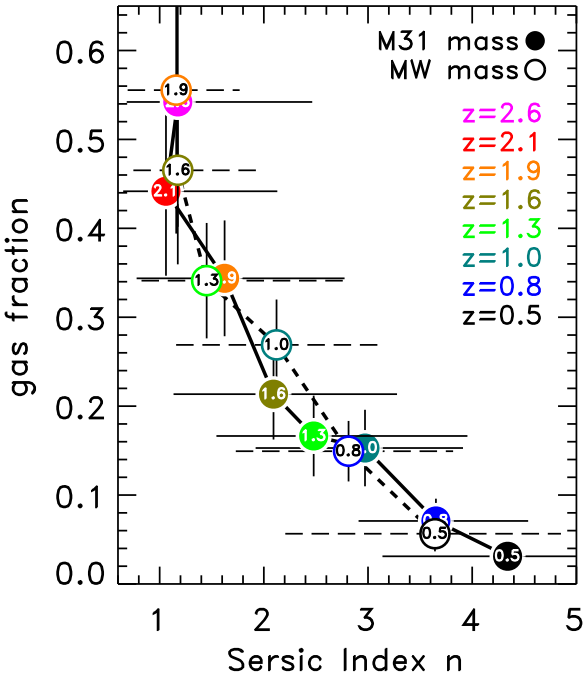

Figure 19. Correlation between the Sérsic index and the implied gas fraction. The measurements for the M31 progenitors are shown as filled circles and solid lines. The measurements for the MW progenitors are shown as open circles and dashed lines. Redshifts are as labeled. There is no difference between the curves, even though they are offset in redshift (see Figure 18), and therefore the decline in the gas fraction is correlated with the increase in galaxy bulges.

It remains an open question why, even at fixed stellar mass, some fraction of the M^* progenitors at fixed redshift are star forming and some are quiescent galaxies. This is similar to the puzzle observed in Kawinwanichakij et al. (2014), who found differences in the number of satellites between star-forming and quiescent central galaxies matched in stellar mass and redshift $1 < z < 3$. This implies that at fixed mass quiescent galaxies have larger-mass halos, and Kawinwanichakij et al. find that a single-halo–mass-quenching threshold is unable to reproduce the galaxy distributions. One conclusion is that while halo mass is the most important driver of galaxy growth and assembly, other factors also play a role (such as environment, local galaxy density, mergers) in determining if a galaxy at fixed stellar mass is quiescent or remains star forming (see also, e.g., Watson et al. 2015).

8.2. Bulge Formation and Morphological Quenching

At $z \lesssim 1$, during the quiescent-transition phase, the M^* galaxies appear to develop bulge/spheroidal components as evidenced by their visual morphology (Figures 12 and 13), and their higher Sérsic-indices at these redshifts (Figure 11). While this process may start as early as $z \sim 2$ for the M31-mass progenitors, this may depend partially on environment. In contrast, there is a marked absence of bulge-dominated ($n_s > 2$) progenitors at high redshift, as was noted in other studies of MW-sized progenitors (e.g., Patel et al. 2013a; van Dokkum et al. 2013).

The emergence of bulges and spheroids occurs during or after the periods of most active star formation. Typical M^*-progenitor galaxies have $n_s \simeq 1$ at early times (highest redshifts). At lower redshifts, we observe on average monotonic increase in the Sérsic index with decreasing redshift starting at $z \sim 2$ for

the M31 progenitors and $z \sim 1.5$ for the MW progenitors that evolves as $n_s \propto (1+z)^{-2}$.

Bruce et al. (2012) show that $n_s = 2$ (3) corresponds approximately to a bulge stellar-mass fraction (bulge-to-total, B/T) of 50% (75%). Therefore, on average, M31- and MW-mass galaxies develop a significant bulge ($n_s = 2$, with presumably B/T = 50%) by $z \simeq 1.7$ and 1.1, respectively; and they develop a dominant bulge ($n_s = 3$, with B/T = 75%) by $z \simeq 1.0$ and 0.7, respectively. However, there is appreciable scatter about the average, and this is likely related to the fact that at any fixed redshift the progenitor population is a mix of star-forming and quiescent galaxies (where the latter presumably have higher n_s).

The formation of spheroids/bulges in the M^* progenitors samples is tied to the transition from star-forming to quiescent phases of the galaxies' evolution. Recent theoretical models connect the formation of stellar spheroids to the dynamics and quenching of star formation in gas-rich, turbulent disks. In these "morphological" quenching (MQ) models the formation of stellar spheroids and stellar-dominated disks stabilize the gas in the galactic disks, suppressing the star formation efficiency (e.g., Bournaud et al. 2007b; Elmegreen et al. 2008; Dekel et al. 2009; Martig et al. 2009; Martig & Bournaud 2010; Ceverino et al. 2010; Genel et al. 2012; Sales et al. 2012; Zavala et al. 2012), and this suppression may be enhanced through an increase in the velocity dispersion of the gas arising from stellar and AGN feedback (also called "Q" quenching, where the increase in velocity dispersion lowers the Toomre Q parameter; see Dekel & Burkert 2014).

Other observational evidence supports the notion that the MQ and Q-quenching processes occur and that quiescent galaxies contain cold reservoirs. Kennicutt (1989) showed that locally, bulge dominated galaxies form stars with lower efficiency than disk-dominated ones. Tumlinson et al. (2013) detected large column densities of cold gas (with low star formation efficiency) in sightlines through the halos of quiescent galaxies. Genzel et al. (2014) provided evidence that this type of quenching occurs in the outer disks of massive, star-forming disk galaxies at high redshift with centrally concentrated mass distributions. This is also consistent with the observations by van Dokkum et al. (2013) and Patel et al. (2013a) who find that galaxies in their sample of MW-mass progenitors form stars in disks at all radii, at least for $z > 0.6$, broadly consistent with expectations from MQ and Q-quenching theories.

The MQ and Q-quenching models are consistent with the anticorrelation between the sSFR and Sérsic index for the M^*-galaxy progenitors. Some MQ and Q-quenching models predict that the galaxies should contain cold gas with low star formation efficiency (e.g., Dekel et al. 2009). This prediction is in line with our results, and plausibly accounts for the discrepancy between the (higher) observed implied gas masses for the M^*-galaxy progenitors and the gas masses measured for local galaxies directly by, e.g., Saintonge et al. (2011). To test these predictions further requires direct measurements of the gas masses of the M^* progenitors at high redshift. How the gas fractions correlate with the Sérsic indices will lead to an understanding of bulge formation and how it affects galaxy formation. This should be testable in part for our sample through future observations from ALMA.

8.3. The Dependence on Stellar Mass

Based on all the observables in this paper, the progenitors of M31-mass and MW-mass galaxies go through all the same stages of evolution, but the higher mass M31-mass progenitors advance through the stages at earlier times (i.e., at higher redshifts) than the lower-mass MW-mass progenitors. Furthermore, the M31-mass progenitors have higher stellar masses at the time they advance to the later evolutionary stages compared to the MW-mass progenitors. It is somewhat remarkable that the M31- and MW-mass progenitors exhibit these evolutionary differences because their present-day stellar masses are separated by only a factor of two. The most obvious explanation for why the M31-mass progenitors begin evolutionary stages sooner is that they have larger halo mass at earlier times (Moster et al. 2013; Behroozi et al. 2013c). If the evolution is driven by the evolution of the mass of the dark-matter halo only, then the stellar-mass/halo-mass ratio evolves strongly with halo mass and redshift. Alternatively, some other process must also be involved.

At the highest redshifts to which we are able to observe the M^* galaxy progenitors ($z \sim 2.5$–3), the SFR and stellar mass grow in tandem. This keeps the sSFR roughly constant (see Figure 16). At this point, the halos in which the M^* progenitors reside accrete gas from the intergalactic medium, and both empirical constraints (e.g., Papovich et al. 2011) and theoretical predictions favor models where the gas accretion is comparable to the SFR (e.g., Neistein et al. 2006; Agertz et al. 2009; Bouché et al. 2010; Ceverino et al. 2010; Dekel et al. 2013; Dekel & Mandelker 2014). The M^* galaxies remain in these "steady-state" (e.g., Dekel et al. 2013) phases until $z \simeq 2.5$ (1.5) for the M31- (MW-)mass progenitors, where the SFR and sSFR then decline at lower redshifts. The decline in the sSFR is similar in form for the two sets of progenitors. However, the decline begins for the M31-mass progenitors when their stellar masses are between $\log M_*/M_\odot = 10.2$ and 10.4, a factor of two to three *higher* than stellar mass of the MW-mass progenitors. This is exactly the same effect as seen in the difference in the evolution of the rest-frame colors and mass for the progenitors of the M31-mass and MW-mass galaxies observed in Figure 8.

The process that begins the suppression of the SFR in M^* progenitors cannot be entirely driven by a simple unevolving halo-mass threshold unless the stellar-mass/halo-mass relation evolves strongly with halo mass and redshift. One possibility is that as the galaxies grow the universe also expands, such that by the time the smaller MW-mass galaxies reach a target stellar mass, the cosmic baryon (and dark-matter) density is lower, which lowers the gas-accretion rate onto halos (see, e.g., Behroozi et al. 2013b). This is conceptually similar to models that find the quenching halo-mass threshold is higher at higher redshift (Dekel & Birnboim 2006), and this may drive evolution in the stellar-mass/halo-mass relation (Moster et al. 2013; Behroozi et al. 2013a).

Therefore, models for the evolution of the star formation efficiency and quenching in galaxies require both a redshift and mass dependence. The mass dependent star formation efficiency is easy to understand in terms of feedback processes, which are stronger when halos are lower mass with shallower gravitational potential wells (e.g., Lu et al. 2014). Another solution may be that gas in the halos of galaxies is preheated by early starbursts or other processes, which delays baryonic accretion onto the galaxies (Lu et al. 2015). This could allow for redshift-dependent effects in the star formation efficiency at fixed halo mass. The redshift-dependence effects would also account for why the lower-mass MW-mass galaxies never attain the same peak SFRs as the higher-mass M31-mass galaxies.

9. SUMMARY

We track the evolution of progenitors of present-day M^* galaxies, selected from abundance-matching methods of $z = 3$ to 0.5. The abundance-matching methods account effects of galaxy formation and mergers. We track the evolution of M^* galaxies at two present-day values of stellar mass, including M31-mass progenitors with present-day stellar masses of $10^{11}\,M_\odot$ and MW-mass progenitors with present-day stellar mass of $5\times10^{10}\,M_\odot$. This allows us to study the mass-dependent evolution for a full range of stellar masses that encompass present-day M^* galaxies, including galaxies like the MW and M31 proper. Furthermore, we are able to study the evolution of galaxies separated by a factor of two in stellar mass.

The data paint a consistent picture of present-day M^* galaxy evolution, and this is based on three independent data sets: the rest-frame $U-V$, $V-J$ color evolution derived from the full 0.3–8.0 μm photometric data sets, the evolution of sizes and Sérsic indices from *HST*/WFC3 imaging, and evolution in the far-IR luminosities as measured from the *Spitzer* and *Herschel* data. There is appreciable scatter in the observed quantities for the progenitors at any redshift (and partly this is because the progenitors of a present-day M^* galaxy have a range of mass at higher redshift; see Behroozi et al. 2013a). Therefore the evolution processes and timescales clearly vary from galaxy to galaxy, and may not apply to individual M^* galaxies. However, for the population, the average evolution of the "typical" progenitor is still very enlightening for the formation of the present-day M^* galaxy population.

All the progenitors of the present-day M^* galaxies go through the same evolutionary stages.

1. At the earliest epochs, the progenitors are blue and star forming, with relatively unattenuated galaxies, with properties similar to LBGs and LAEs. This is therefore the "LBG phase." The morphologies have disk-like exponential surface-brightness profiles (Sérsic index $n_s = 1$) that grow as $H(z)^{-1}$, as expected for the smooth growth of the dark-matter halos (at least under the assumption of a constant halo spin parameter). For the M31-mass progenitors this phase extends to $z \gtrsim 2.5$, and for the MW-mass progenitors this phase occurs at $z \gtrsim 2$.
2. At later times, the "typical" progenitor becomes an IR-luminous star-forming galaxy with higher dust obscuration. This is observed in the evolution of the median rest-frame colors and the median IR luminosity. For M31-mass progenitors this phase begins around $z = 2.5$ and continues to $z \sim 1.5$, with a peak SFR of $\Psi = 50\,M_\odot$ yr^{-1} from $z \sim 2.5$ to $z \sim 1.8$. For MW-mass progenitors the IR luminous phase begins later, from $z \sim 1.8$ to $z \sim 1.0$, with a peak SFR of $\Psi = 30\,M_\odot$ yr^{-1} around $z \sim 1.5$. This is the "luminous IR galaxy" phase of M^*-galaxy evolution.
3. During the "luminous IR galaxy" phase the Sérsic index increases from $n_s \simeq 1$ at a rate of roughly $n_s \propto (1+z)^{-2}$ starting at $z \sim 2$ for the M31-mass galaxies and $z \sim 1.5$ for the MW-mass galaxies. The M^* galaxies appear to populate the well-known "Hubble sequence" by $z \sim 1$. The fraction of quiescent galaxies also rises with decreasing redshift in tandem with the Sérsic index evolution (and therefore bulge growth) such that when $n_s \simeq 2$ the quiescent fraction is approximately 50%. This is accompanied with a decline in the sSFR.
4. At the latest times (lowest redshifts), the SFR for both the M31-mass and MW-mass progenitors show a steady decline, most pronounced for $z < 1$. During this period the Sérsic indices continue to increase with decreasing redshift and the quiescent fraction increases such that the typical M31-mass progenitor has $n_s = 3.6$ with a quiescent fraction of 70% at $z = 0.8$. The typical MW-mass progenitor evolution is delayed and it reaches these values at $z \sim 0.5$. This stage is the "quiescent transition" phase. The majority of present-day M^* galaxies should be quiescent, and this seems consistent with observations (although it may be that the MW and M31 proper are outliers; see Mutch et al. 2011).

While the M31-mass and MW-mass progenitors experience the same evolutionary phases, the M31-mass galaxies experience them sooner (higher redshift) with higher relative stellar mass compared to the MW-mass progenitors. This means the threshold mass for any quenching process depends on redshift (and therefore the stellar-mass/halo-mass relation is evolving) and may be related to physical processes motivated by models, including lower gas accretion rate, an evolving magnitude of galaxy feedback, preheating of baryonic gas in galaxy halos, and lower cosmic density of baryons as the universe evolves.

Our observations show that the formation of bulges in M^* galaxies (as measured from the Sérsic indices) is simultaneous with a decline in the inferred cold gas mass (implied by inverting the Kennicutt–Schmidt law), and suggests these processes are related. Because the evolution in these quantities is smooth for the "typical" M^*-galaxy progenitor, this favors slower acting processes that drive the transition from gas-rich (star-forming) disk galaxy to quiescent, bulge-dominated galaxy, rather than dramatic, stochastic processes, like major mergers, as a dominant driver for this evolution, unless the timescales for the latter are so short that the median evolution remains smooth. Our observations are consistent with ideas in MQ and Q-quenching models. These predict generically that the growth of stellar bulges and disks stabilize cold gas against fragmentation, perhaps combined with an increase in gas turbulence from stellar/AGN feedback, which lowers the Toomre Q parameter.

One test for understanding the evolution of M^* progenitors will come from measurements of the cold-gas mass (and the gas-mass/stellar-mass ratio) from observations with facilities such as ALMA. If the gas fractions are as low as implied here from the SFR and sizes of the galaxies, then the processes driving the transition of a star-forming galaxy to a quiescent, bulge-dominated galaxy must remove the gas from the systems. In contrast, if processes stabilize the gas against instabilities, then the galaxies will have higher measured cold-gas fractions with low star formation efficiencies, which will favor MQ and Q-quenching models. Correlating these cold-gas measurements with galaxy morphological properties (such as the bulge/total ratio) will test the details of these theories.

We thank our other colleagues in CANDELS and ZFOURGE for their work and collaboration. We thank B. Moster for valuable input, and we thank the referee for a thorough report that improved the quality and clarity of this paper. This work is supported by the National Science Foundation through grants AST-1009707 and AST-0808133. I.L. acknowledges support from ERC HIGHZ 227749 and NL-NWO Spinoza. This work is based on observations taken by the CANDELS Multi-Cycle Treasury Program with the NASA/ESA *HST*, which is operated by the Association of Universities for Research in Astronomy, Inc., under NASA contract NAS5-26555. This work is supported in part by *HST* program number GO-12060. Support for Program number GO-12060 was provided by

NASA through a grant from the Space Telescope Science Institute, which is operated by the Association of Universities for Research in Astronomy, Incorporated, under NASA contract NAS5-26555. This work is based on observations made with the *Spitzer Space Telescope*, which is operated by the Jet Propulsion Laboratory, California Institute of Technology. This work is based on observations made with the *Herschel Space Observatory*. *Herschel* is an ESA space observatory with science instruments provided by European-led Principal Investigator consortia and with important participation from NASA. This paper includes data gathered with the 6.5 m Magellan Telescopes located at Las Campanas Observatory, Chile. Australian access to the Magellan Telescopes was supported through the National Collaborative Research Infrastructure Strategy of the Australian Federal Government. We acknowledge generous support from the Texas A&M University and the George P. and Cynthia Woods Institute for Fundamental Physics and Astronomy. This paper is dedicated to the memory of Alma J. Broy and James W. Broy of Baltimore, Maryland.

REFERENCES

Agertz, O., Teyssier, R., & Moore, B. 2009, MNRAS, 397, L64
Baldry, I. K., Glazebrook, K., & Driver, S. P. 2008, MNRAS, 388, 945
Bassett, R., Papovich, C., Lotz, J. M., et al. 2013, ApJ, 770, 58
Behroozi, P. S., Conroy, C., & Wechsler, R. H. 2010, ApJ, 717, 379
Behroozi, P. S., Marchesini, D., Wechsler, R. H., et al. 2013a, ApJL, 777, L10
Behroozi, P. S., Wechsler, R. H., & Conroy, C. 2013b, ApJL, 762, L31
Behroozi, P. S., Wechsler, R. H., & Conroy, C. 2013c, ApJ, 770, 57
Bell, E. F. 2003, ApJ, 586, 794
Bell, E. F., McIntosh, D. H., Katz, N., & Weinberg, M. D. 2003, ApJS, 149, 289
Bell, E. F., Papovich, C., Wolf, C., et al. 2005, ApJ, 625, 23
Bell, E. F., van der Wel, A., Papovich, C., et al. 2012, ApJ, 753, 167
Bezanson, R., van Dokkum, P. G., Franx, M., et al. 2011, ApJL, 737, L31
Bouché, N., Dekel, A., Genzel, R., et al. 2010, ApJ, 718, 1001
Bournaud, F., Elmegreen, B. G., & Elmegreen, D. M. 2007a, ApJ, 670, 237
Bournaud, F., Jog, C. J., & Combes, F. 2007b, A&A, 476, 1179
Brammer, G. B., van Dokkum, P. G., & Coppi, P. 2008, ApJ, 686, 1503
Brammer, G. B., Whitaker, K. E., van Dokkum, P. G., et al. 2011, ApJ, 739, 24
Brinchmann, J., Charlot, S., Heckman, T. M., et al. 2004, arXiv:astro-ph/0406220
Brown, M. J. I., Dey, A., Jannuzi, B. T., et al. 2007, ApJ, 654, 858
Brown, M. J. I., Zheng, Z., White, M., et al. 2008, ApJ, 682, 937
Bruce, V. A., Dunlop, J. S., Cirasuolo, M., et al. 2012, MNRAS, 427, 1666
Bruzual, G., & Charlot, S. 2003, MNRAS, 344, 1000
Bundy, K., Fukugita, M., Ellis, R. S., et al. 2009, ApJ, 697, 1369
Calzetti, D., Armus, L., Bohlin, R. C., et al. 2000, ApJ, 533, 682
Cardamone, C. N., Urry, C. M., Schawinski, K., et al. 2010, ApJL, 721, L38
Ceverino, D., Dekel, A., & Bournaud, F. 2010, MNRAS, 404, 2151
Ceverino, D., Dekel, A., Mandelker, N., et al. 2012, MNRAS, 420, 3490
Chabrier, G. 2003, PASP, 115, 763
Chary, R., & Elbaz, D. 2001, ApJ, 556, 562
Conselice, C. J., Mortlock, A., Bluck, A. F. L., Grützbauch, R., & Duncan, K. 2013, MNRAS, 430, 1051
Cool, R. J., Eisenstein, D. J., Fan, X., et al. 2008, ApJ, 682, 919
Daddi, E., Bournaud, F., Walter, F., et al. 2010, ApJ, 713, 686
Dale, D. A., Bendo, G. J., Engelbracht, C. W., et al. 2005, ApJ, 633, 857
de Rossi, M. E., Tissera, P. B., De Lucia, G., & Kauffmann, G. 2009, MNRAS, 395, 210
Dekel, A., & Birnboim, Y. 2006, MNRAS, 368, 2
Dekel, A., & Burkert, A. 2014, MNRAS, 438, 1870
Dekel, A., & Mandelker, N. 2014, MNRAS, 444, 2071
Dekel, A., Sari, R., & Ceverino, D. 2009, ApJ, 703, 785
Dekel, A., Zolotov, A., Tweed, D., et al. 2013, MNRAS, 435, 999
Delaye, L., Huertas-Company, M., Mei, S., et al. 2014, MNRAS, 441, 203
Dole, H., Lagache, G., Puget, J.-L., et al. 2006, A&A, 451, 417
Dye, S., Eales, S. A., Ashby, M. L. N., et al. 2007, MNRAS, 375, 725
Elbaz, D., Dickinson, M., Hwang, H. S., et al. 2011, A&A, 533, A119
Elmegreen, B. G., Bournaud, F., & Elmegreen, D. M. 2008, ApJ, 688, 67
Erb, D. K., Steidel, C. C., Shapley, A. E., et al. 2006, ApJ, 646, 107
Ferguson, H. C., Dickinson, M., Giavalisco, M., et al. 2004, ApJL, 600, L107
Flynn, C., Holmberg, J., Portinari, L., Fuchs, B., & Jahreiß, H. 2006, MNRAS, 372, 1149
Förster-Schreiber, N. M., Genzel, R., Bouché, N., et al. 2009, ApJ, 706, 1364
Förster Schreiber, N. M., Shapley, A. E., Erb, D. K., et al. 2011, ApJ, 731, 65
Franx, M., van Dokkum, P. G., Schreiber, N. M. F., et al. 2008, ApJ, 688, 770
Fumagalli, M., Patel, S. G., Franx, M., et al. 2012, ApJL, 757, L22
Gallazzi, A., & Bell, E. F. 2009, ApJS, 185, 253
Gawiser, E., Francke, H., Lai, K., et al. 2007, ApJ, 671, 278
Geehan, J. J., Fardal, M. A., Babul, A., & Guhathakurta, P. 2006, MNRAS, 366, 996
Genel, S., Dekel, A., & Cacciato, M. 2012, MNRAS, 425, 788
Genzel, R., Burkert, A., Bouché, N., et al. 2008, ApJ, 687, 59
Genzel, R., Förster Schreiber, N. M., Lang, P., et al. 2014, ApJ, 785, 75
Giavalisco, M. 2002, ARA&A, 40, 579
Giavalisco, M., Ferguson, H. C., Koekemoer, A. M., et al. 2004, ApJL, 600, L93
Giavalisco, M., Vanzella, E., Salimbeni, S., et al. 2011, ApJ, 743, 95
Gibbons, S. L. J., Belokurov, V., & Evans, N. W. 2014, MNRAS, 445, 3788
Grogin, N. A., Kocevski, D. D., Faber, S. M., et al. 2011, ApJS, 197, 35
Hammer, F., Puech, M., Chemin, L., Flores, H., & Lehnert, M. D. 2007, ApJ, 662, 322
Huynh, M. T., Pope, A., Frayer, D. T., & Scott, D. 2007, ApJ, 659, 305
Ilbert, O., McCracken, H. J., Le Fèvre, O., et al. 2013, A&A, 556, A55
Jogee, S., Miller, S., Penner, K., et al. 2008, in ASP Conf. Ser. 396, Formation and Evolution of Galaxy Disks, ed. J. G. Funes & E. M. Corsini (San Francisco, CA: ASP), 337
Karim, A., Schinnerer, E., Martnez-Sansigre, A., et al. 2011, ApJ, 730, 61
Kauffmann, G., Heckman, T. M., White, S. D. M., et al. 2003, MNRAS, 341, 54
Kauffmann, G., White, S. D. M., Heckman, T. M., et al. 2004, MNRAS, 353, 713
Kawinwanichakij, L., Papovich, C., Quadri, R. F., et al. 2014, ApJ, 792, 103
Kennicutt, R. C., Jr. 1989, ApJ, 344, 685
Kennicutt, R. C., Jr. 1998a, ARA&A, 36, 189
Kennicutt, R. C., Jr. 1998b, ApJ, 498, 541
Kocevski, D. D., Faber, S. M., Mozena, M., et al. 2012, ApJ, 744, 148
Koekemoer, A. M., Faber, S. M., Ferguson, H. C., et al. 2011, ApJS, 197, 36
Komatsu, E., Smith, K. M., Dunkley, J., et al. 2011, ApJS, 192, 18
Kormendy, J., Bender, R., & Cornell, M. E. 2011, Natur, 469, 374
Kriek, M., van Dokkum, P. G., Labbé, I., et al. 2009, ApJ, 700, 221
Kurk, J., Cimatti, A., Zamorani, G., et al. 2009, A&A, 504, 331
Labbé, I., Bouwens, R., Illingworth, G. D., & Franx, M. 2006, ApJL, 649, L67
Labbé, I., Gonzlez, V., Bouwens, R. J., et al. 2010, ApJL, 716, L103
Labbé, I., Huang, J., Franx, M., et al. 2005, ApJL, 624, L81
Lee, K., Dey, A., Reddy, N., et al. 2011, ApJ, 733, 99
Lee, N., Le Floc'h, E., Sanders, D. B., et al. 2010, ApJ, 717, 175
Leitner, S. N. 2012, ApJ, 745, 149
Leja, J., van Dokkum, P., & Franx, M. 2013, ApJ, 766, 33
Licquia, T. C., & Newman, J. A. 2014, ApJ, submitted (arXiv:1407.1078)
Lu, Y., Mo, H. J., & Wechsler, R. H. 2015, MNRAS, 446, 1907
Lu, Y., Wechsler, R. H., Somerville, R. S., et al. 2014, ApJ, 795, 123
Lundgren, B. F., van Dokkum, P., Franx, M., et al. 2014, ApJ, 780, 34
Magnelli, B., Elbaz, D., Chary, R. R., et al. 2011, A&A, 528, A35
Magnelli, B., Popesso, P., Berta, S., et al. 2013, A&A, 553, A132
Maraston, C., Pforr, J., Renzini, A., et al. 2010, MNRAS, 407, 830
Marchesini, D., Muzzin, A., Stefanon, M., et al. 2014, ApJ, 794, 65
Marchesini, D., van Dokkum, P. G., Förster Schreiber, N. M., et al. 2009, ApJ, 701, 1765
Martig, M., & Bournaud, F. 2010, ApJL, 714, L275
Martig, M., Bournaud, F., Teyssier, R., & Dekel, A. 2009, ApJ, 707, 250
McMillan, P. J. 2011, MNRAS, 414, 2446
Mo, H. J., Mao, S., & White, S. D. M. 1998, MNRAS, 295, 319
Morganti, R., de Zeeuw, P. T., Oosterloo, T. A., et al. 2006, MNRAS, 371, 157
Morishita, T., Ichikawa, T., & Kajisawa, M. 2014, ApJ, 785, 18
Moster, B. P., Naab, T., & White, S. D. M. 2013, MNRAS, 428, 3121
Moustakas, J., Coil, A. L., Aird, J., et al. 2013, ApJ, 767, 50
Mutch, S. J., Croton, D. J., & Poole, G. B. 2011, ApJ, 736, 84
Muzzin, A., Marchesini, D., Stefanon, M., et al. 2013, ApJ, 777, 18
Neistein, E., van den Bosch, F. C., & Dekel, A. 2006, MNRAS, 372, 933
Nilsson, K. K., Östlin, G., Møller, P., et al. 2011, A&A, 529, A9
Noeske, K. G., Weiner, B. J., Faber, S. M., et al. 2007, ApJL, 660, L43
Oke, J. B., & Gunn, J. E. 1983, ApJ, 266, 713
Pacifici, C., Kassin, S. A., Weiner, B., et al. 2013, ApJ, 762, L15
Pacifici, C., da Cunha, E., Charlot, S., et al. 2015, MNRAS, 447, 790
Papovich, C., Bassett, R., Lotz, J. M., et al. 2012, ApJ, 750, 93
Papovich, C., Dickinson, M., & Ferguson, H. C. 2001, ApJ, 559, 620
Papovich, C., Dickinson, M., Giavalisco, M., Conselice, C. J., & Ferguson, H. C. 2005, ApJ, 631, 101

Papovich, C., Finkelstein, S. L., Ferguson, H. C., Lotz, J. M., & Giavalisco, M. 2011, MNRAS, 412, 1123
Papovich, C., Moustakas, L. A., Dickinson, M., et al. 2006, ApJ, 640, 92
Papovich, C., Rudnick, G., Le Floc'h, E., et al. 2007, ApJ, 668, 45
Patel, S. G., Fumagalli, M., Franx, M., et al. 2013a, ApJ, 778, 115
Patel, S. G., van Dokkum, P. G., Franx, M., et al. 2013b, ApJ, 766, 15
Persson, S. E., Murphy, D. C., Smee, S., et al. 2013, PASP, 125, 654
Popesso, P., Magnelli, B., Buttiglione, S., et al. 2012, A&A, submitted (arXiv:1211.4257)
Reddy, N. A., Erb, D. K., Pettini, M., Steidel, C. C., & Shapley, A. E. 2010, ApJ, 712, 1070
Reddy, N. A., Pettini, M., Steidel, C. C., et al. 2012, ApJ, 754, 25
Rieke, G. H., Alonso-Herrero, A., Weiner, B. J., et al. 2009, ApJ, 692, 556
Rix, H.-W., & Bovy, J. 2013, A&ARv, 21, 61
Rodighiero, G., Cimatti, A., Gruppioni, C., et al. 2010, A&A, 518, L25
Saintonge, A., Kauffmann, G., Kramer, C., et al. 2011, MNRAS, 415, 32
Sales, L. V., Navarro, J. F., Theuns, T., et al. 2012, MNRAS, 423, 1544
Schmidt, M. 1959, ApJ, 129, 243
Schreiber, C., Pannella, M., Elbaz, D., et al. 2014, A&A, in press (arXiv:1409.5433)
Shapley, A. E. 2011, ARA&A, 49, 525
Shapley, A. E., Steidel, C. C., Adelberger, K. L., et al. 2001, ApJ, 562, 95
Shipley, H. V., Papovich, C., Rieke, G. H., et al. 2013, ApJ, 769, 75
Skelton, R. E., Whitaker, K. E., Momcheva, I. G., et al. 2014, ApJS, 214, 24
Spitler, L. R., Labbé, I., Glazebrook, K., et al. 2012, ApJL, 748, L21
Steidel, C. C., Adelberger, K. L., Giavalisco, M., Dickinson, M., & Pettini, M. 1999, ApJ, 519, 1
Stewart, K. R., Bullock, J. S., Barton, E. J., & Wechsler, R. H. 2009, ApJ, 702, 1005
Tacconi, L. J., Genzel, R., Neri, R., et al. 2010, Natur, 463, 781
Tacconi, L. J., Neri, R., Genzel, R., et al. 2013, ApJ, 768, 74
Tal, T., Dekel, A., Oesch, P., et al. 2014, ApJ, 789, 164
Taylor, E. N., Franx, M., van Dokkum, P. G., et al. 2009, ApJS, 183, 295
Tilvi, V., Papovich, C., Tran, K.-V. H., et al. 2013, ApJ, 768, 56
Tomczak, A. R., Quadri, R. F., Tran, K.-V. H., et al. 2014, ApJ, 783, 85
Tumlinson, J., Thom, C., Werk, J. K., et al. 2013, ApJ, 777, 59
van der Wel, A., Bell, E. F., Häussler, B., et al. 2012, ApJS, 203, 24
van der Wel, A., Franx, M., van Dokkum, P. G., et al. 2014, ApJ, 788, 28
van Dokkum, P. G., Labb, I., Marchesini, D., et al. 2009, PASP, 121, 2
van Dokkum, P. G., Leja, J., Nelson, E. J., et al. 2013, ApJL, 771, L35
van Dokkum, P. G., Whitaker, K. E., Brammer, G., et al. 2010, ApJ, 709, 1018
Vargas, C. J., Bish, H., Acquaviva, V., et al. 2014, ApJ, 783, 26
Watson, D. F., Hearin, A. P., Berlind, A. A., et al. 2015, MNRAS, 446, 651
Whitaker, K. E., Labbé, I., van Dokkum, P. G., et al. 2011, ApJ, 735, 86
Williams, R. J., Quadri, R. F., Franx, M., van Dokkum, P., & Labbé, I. 2009, ApJ, 691, 1879
Wuyts, S., Labb, I., Franx, M., et al. 2007, ApJ, 655, 51
Young, L. M., Bendo, G. J., & Lucero, D. M. 2009, AJ, 137, 3053
Zavala, J., Avila-Reese, V., Firmani, C., & Boylan-Kolchin, M. 2012, MNRAS, 427, 1503
Zheng, X. Z., Bell, E. F., Rix, H., et al. 2006, ApJ, 640, 784
Zheng, X. Z., Dole, H., Bell, E. F., et al. 2007, ApJ, 670, 301